

Characterization of Infrared Dark Clouds[★]

NH₃ Observations of an Absorption-contrast Selected IRDC Sample

R.-A. Chira¹, H. Beuther¹, H. Linz¹, F. Schuller², C. M. Walmsley^{3,4}, K. M. Menten⁵, and L. Bronfman⁶

¹ Max-Planck Institute for Astronomy, MPIA, Königstuhl 17, 69117 Heidelberg, Germany
e-mail: rox.chira@gmail.com

² European Southern Observatory, Alonso de Cordova 3107, Casilla 19001, Santiago 19, Chile

³ Osservatorio Astrofisico di Arcetri, Largo E. Fermi 5, I-50125 Firenze, Italy

⁴ Dublin Institute for Advanced Studies (DIAS), 31 Fitzwilliam Place, Dublin 2, Ireland

⁵ Max-Planck-Institute for Radioastronomy, Auf dem Hügel 69, D-53121 Bonn, Germany

⁶ Departamento de Astronomia, Universidad de Chile, Casilla 36-D, Santiago, Chile

Submitted 09.05.2012, Accepted 18.12.2012

Abstract

Context. Despite increasing research in massive star formation, little is known about its earliest stages. Infrared Dark Clouds (IRDCs) are cold, dense and massive enough to harbour the sites of future high-mass star formation. But up to now, mainly small samples have been observed and analysed.

Aims. To understand the physical conditions during the early stages of high-mass star formation, it is necessary to learn more about the physical conditions and stability in relatively unevolved IRDCs. Thus, for characterising IRDCs studies of large samples are needed.

Methods. We investigate a complete sample of 218 northern hemisphere high-contrast IRDCs using the ammonia (1,1)- and (2,2)-inversion transitions.

Results. We detected ammonia (1,1)-inversion transition lines in 109 of our IRDC candidates. Using the data we were able to study the physical conditions within the star-forming regions statistically. We compared them with the conditions in more evolved regions which have been observed in the same fashion as our sample sources. Our results show that IRDCs have, on average, rotation temperatures of 15 K, are turbulent (with line width FWHMs around 2 km s⁻¹), have ammonia column densities on the order of 10¹⁴ cm⁻² and molecular hydrogen column densities on the order of 10²² cm⁻². Their virial masses are between 100 and a few 1000 M_⊙. The comparison of bulk kinetic and potential energies indicate that the sources are close to virial equilibrium.

Conclusions. IRDCs are on average cooler and less turbulent than a comparison sample of high-mass protostellar objects, and have lower ammonia column densities. Virial parameters indicate that the majority of IRDCs are currently stable, but are expected to collapse in the future.

Key words. Stars: formation – IMF: clouds – IMF: molecules – IMF: abundances

1. Introduction

Despite their relatively small numbers, massive stars are important components of galaxies. However, we know little about the initial conditions for the formation of high-mass stars due to the difficulty of identifying the sites at which they form. Early stages of massive star formation should contain cold gas and dust cores with a peak in the spectral energy distribution around 200 μm and no emission at near- and mid-infrared wavelengths. Using near- to mid-infrared Galactic Plane surveys from the Midcourse Space Experiment (MSX), the Infrared Space Observatory (ISO) and the Spitzer Space Observatory, it is possible to identify large samples of Infrared Dark Clouds (IRDCs). These are dark, compact silhouettes seen against strong Galactic Background emission (Simon et al. 2006; Peretto & Fuller 2009; Perault et al. 1996; Egan et al. 1998). IRDCs have high molecular hydrogen column densities (~ 10²² cm⁻², Simon et al. 2006) and block background radiation, in particular at opti-

cal and near-infrared wavelengths. They cover broad ranges of gas masses from low-mass to high-mass star-forming regions. The IRDCs on the upper end of gas mass range are considered to be capable of harbouring high-mass star-forming regions in their earliest evolutionary stages. Based on the MSX database, Simon et al. (2006) built up a catalogue of about 10,000 candidate IRDCs which are excellent starting points for studies of the early stages of high-mass star formation. Since this catalogue is only based on mid-infrared absorption images, it lacks any additional information about the physical conditions within these regions. Therefore, further studies are needed. In this work we investigate the temperatures, turbulent properties and the virial parameters of IRDCs using the ammonia (NH₃) (*J, K*) = (1,1)- and (2,2)-inversion transitions. Ammonia has critical densities on the order of 10³ cm⁻³ and so its radio wavelength inversion transitions are good higher-density tracers which suffer from minimal freeze out (Bergin & Tafalla 2007). The (1,1)- and (2,2)-inversion lines can be observed simultaneously making ammonia also a good thermometer (Walmsley & Ungerechts 1983). Since radiative transitions between different K-ladders are forbidden, metastable (J,K)-inversion level (with J = K) are only populated

[★] Full derivations in Appendix A and Figures in B are published online only. Full Tables C.1-C.4 are only available at the CDS via anonymous ftp to cdsarc.u-strasbg.fr (130.79.128.5) or via <http://cdsarc.u-strasbg.fr/viz-bin/qcat?J/A+A/>

via collisions (Ho & Townes 1983). From the observed ammonia spectra it is possible to determine a source's kinetic temperatures (Walmsley & Ungerechts 1983), the level of turbulence via the line widths and its virial mass. Using the lines' rest velocities we can also calculate the kinematic distances of the sources using a model of the Galactic rotation curve (Reid et al. 2009).

Ammonia studies analysing star-forming gas clumps have also been conducted for less massive sources (e.g. Harju et al. 1991, 1993). It has been observed in high-mass regions for decades (Churchwell et al. 1990; Molinari et al. 1996; Sridharan et al. 2002; Schreyer et al. 1996), but most previous studies discussed smaller and/or more evolved samples (e.g., Sridharan et al. 2005; Pillai et al. 2006). The advantage of our sample is that it is large enough to study the physical properties of IRDCs statistically. Thus, we can compare our results to studies of objects in more evolved stages of high-mass star formation. In particular, we compare the physical conditions found in IRDCs with those in High-Mass Protostellar Objects (HMPOs, by Sridharan et al. 2002). HMPOs comprise the next evolutionary stage where at the core centres massive protostars have formed already. Typical luminosities exceed $10^4 L_{\odot}$ and accretion processes are likely still ongoing (Sridharan et al. 2002).

Furthermore, the ammonia data will be compared with data on submm wavelength ($870 \mu\text{m}$) dust emission collected in the course of the ATLASGAL (the Atacama Pathfinder Experiment Telescope Large Area Survey of the Galaxy) survey (Schuller et al. 2009). With this additional data, we will be able to determine the sources gas masses, molecular hydrogen column densities and ammonia abundances and gain information about the stability of IRDCs.

Recently, Dunham et al. (2011) and Wienen et al. (2012) presented their works. They studied more heterogeneous samples (concerning the evolutionary stages of star formation in the observed regions) based on BOLOCAM and ATLASGAL (Rosolowsky et al. 2010; Schuller et al. 2009). Although they did not focus on IRDCs as we did, they have corresponding subsamples with sources at typical distances similar to ours. Thus, we will discuss similarities and differences between these studies and ours as well.

Further details about the selection criteria of our IRDC sample, the observations, data reduction and analysis are given in the Sects. 2 - 4. In Sect. 4, the IRDCs' rotation and kinetic temperatures, and column densities of ammonia are derived and compared with the data of the HMPO sample by Sridharan et al. (2002). Furthermore, we study the molecular hydrogen column density and ammonia abundance, as well as the stability of the IRDCs by analysing their virial parameters.

The paper is outlined as follows. Sect. 2 introduces details about

our sample and the selection criteria. Sect. 3 provides information about the observations and data reduction. In Sect. 4 we present and discuss our results. In Sect. 5 we summarise them and state our conclusions.

2. Source Sample

Based on the $8.3 \mu\text{m}$ data collected by the MSX, Simon et al. (2006) compiled a catalogue of more than 10,000 candidate IRDCs. Those contain about 12,000 embedded Infrared Dark Cores that appear as high-contrast peaks within the IRDCs. We specifically selected Cores and refer to them here as IRDCs. In an attempt to present a complete sample of the northern hemisphere high-contrast IRDCs, our sample of 218 sources

was selected from the catalogue of Simon et al. (2006) based on the following criteria.

Firstly, the sources had to have contrast values greater than 0.3, where contrast is defined as $\text{contrast} = (\text{background} - \text{image}) / \text{background}$ (see Simon et al. 2006). This selects clouds with column densities of the order of 10^{22} cm^{-2} of molecular hydrogen or 10^{14} cm^{-2} of ammonia. For a source to be considered significant, the ratio of the peak-contrast versus its uncertainty has to be larger than three. Secondly, the sources needed to be observable from Effelsberg for more than five hours and be larger than 0.6 arcmin^2 to fill the beam of $40''$ FWHM at the given frequencies. Therefore, they have to be above an elevation of 20° corresponding to Galactic Longitudes roughly larger than 19° . Thus, our systematic analysis of our sample started at $l = 19.27^\circ$ (it was also possible to observe nine sources with $l < 19^\circ$ which are exceptions). The coordinates of the IRDCs we used, were taken from the catalogue based on the MSX observations (Simon et al. 2006). We see small differences compared to studies using (sub)mm peak positions. For consistency, we used the same positions for the ATLASGAL and Spitzer maps (cf. Sect. 4.5.2 and Sect. 4.5.4).

3. Observation and Data

In 2008 and 2009, we used the Effelsberg 100 m telescope to observe simultaneously the NH_3 (1,1)- and (2,2)- inversion lines with central rest frequencies of 23.6945 and 23.7226 GHz, respectively. The data were taken in a frequency switching mode with on average five minutes integration time per position. The weather was adequate with system temperatures mostly below 50 K. The full width half maximum (FWHM) is $40''$ and the velocity resolution is $\Delta v = 0.38 \text{ km s}^{-1}$. The absolute flux calibration was determined from observations of NGC 7027.

Fitting the whole hyperfine structure (HFS) of both lines using the standard procedures of CLASS (Hily-Blant et al. 2006), the brightness temperatures, T_{mb} , local standard of rest velocities, V_{lsr} , line width FWHMs, Δv , and optical depths, τ , were derived. The results are listed in Table C.1.

One has to consider that the HFS satellites, especially of the (2,2) transition, have not been detected in every spectrum. This will be discussed in Sect. 4.1.1.

Table 1: Number of sources being eliminated by the individual selection criteria.

Selection Criterion	Number of eliminated Sources ^a
(a) NH_3 (1,1) line detected	91
(b) $8 < T_{\text{rot}} < 50 \text{ K}$	17
(c) $F_{870\mu\text{m}}^{40''} > 4 \text{ RMS}$	8

^a Note that some sources have been eliminated, because they did not fulfil several of these criteria. Therefore, the sum of the listed sources here is bigger than the 109 sources which have been actually eliminated.

4. Results

4.1. Distribution of Detected IRDCs within the Galactic Plane

4.1.1. Detection Rate

Out of our original sample of 218 sources 109 were detected in ammonia. The fit parameters of the sources with detected am-

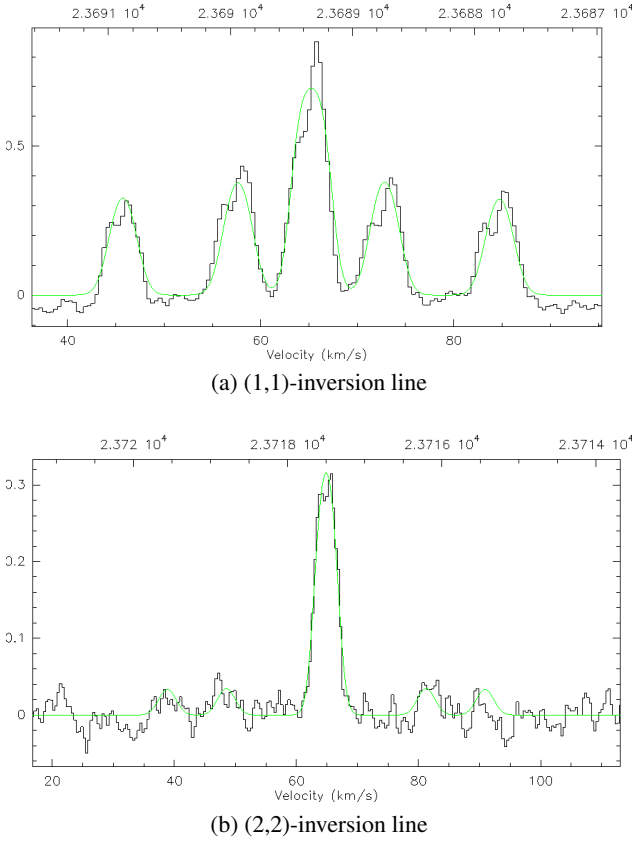


Figure 1: Example for a good detection in ammonia. NH_3 inversion lines in G19.92-00.29A. The green line indicates the hyperfine fit by CLASS.

monia inversion transitions are listed in Tables C.1 to C.3 in the Appendix. The formal errors (1σ) for the calculated quantities have been derived from Gaussian error propagation. IRDCs positions are indicated in Figs. B.1 and B.2 (cf. Appendix). The black-and-white background is taken from the ATLASGAL dust emission maps by Schuller et al. (2009). The figures show a relatively good agreement between the compact sources detected by MSX extinction and by ATLASGAL.

For our analysis we applied the following criteria to obtain the significance of the statistics.

(a) The (1,1)-inversion line is detected and the brightness temperatures are higher than the threefold root-mean-square (RMS).
(b) The rotation temperatures are between 8 K and 50 K and the absolute errors are lower than 20 K. This is necessary, because both inversion lines are sensible temperature indicators, but only within this range (Danby et al. 1988).

(c) The flux densities $F_{\nu}^{40''}$ of the IRDCs' counterparts in the ATLASGAL dust emission maps are greater than four times the RMS noise. This last criterion is needed for the virial analysis (cf. Sect. 4.5). In this case we were not able to derive independent gas masses or hydrogen column densities. If a source fulfils the first two criteria, but not the last one, its NH_3 properties - rotation and kinetic temperatures, column densities of ammonia and the virial masses (Schilke 1989; Ho & Townes 1983; MacLaren et al. 1988) - have been calculated, anyway, but not the virial parameter, hydrogen column density and ammonia abundance.

A good example for a detection fulfilling all of these criteria is G19.92-00.29A which is shown in Fig. 1. The green lines repre-

sent the fits to the HFS lines determined by CLASS.

81 out of 218 sources satisfied all our criteria. There were 29 sources without detectable (2,2)-inversion lines although the (1,1)-inversion lines was detected. In this case, it is not possible to derive exact parameters. But it is possible to give upper limits for the rotation temperature by using three-times the average RMS noise (0.0925 K, cf. Sect. A.1) as an upper limit for the (2,2)-line intensity (following Ho & Townes 1983, cf. Sect. 4.2). In 91 sources the ammonia inversion transitions are not detected. For the sources not satisfying criterion (a) it is not possible to do any further calculations and analysis. There are 25 spectra with (1,1)-inversion lines lying within the noise. In this case the hyperfine fits by CLASS were not of good quality. A list of all sources toward which ammonia could not be detected is given in Table C.4.

17 sources were dropped, because their calculated rotation temperatures were not between 8 and 50 K. This could be caused by poor signal-to-noise ratios and large errors in the hyperfine structure fits (cf. criterion (a)).

Eight sources turned out to have no significant counterparts in the ATLASGAL dust emission maps. As explained before we used the ammonia data to calculate temperatures, line widths and ammonia column densities for these sources and we list them in the tables in Appendix C.

Our sample and that of Wienen et al. (2012) have very little overlap. Depending on the search radii (defining the area around our sources where we searched corresponding sources of Wienen et al. 2012; in our case 20'', 40'', or 60'') we find 10, 16, or 22 sources in common. The properties derived by Wienen et al. (2012) match our results for the corresponding sources.

Our NH_3 detection rate is 50%. This lower than rates of 87% and 72% (respectively from Wienen et al. 2012 and Dunham et al. 2011) for samples which based on (sub)mm emission data. This indicates that sample selection solely based on mid-infrared absorption studies against the Galactic background are less reliable. Even if a contrast criterion is enforced, such studies can pick up a variety of structures that emulate IRDCs but might often turn out to be blown-out bubbles with very little dense gas inside (e.g. Wilcock et al. 2012). Comprehensive (sub)mm emission studies were not available at the time of our sample selection. The best future sample selections will be most likely based on a combination of mid-infrared absorption and (sub)mm emission selection criteria.

4.1.2. Distribution within the Galactic Plane

Fig. 2 shows the positions of the selected sources within the Galactic Plane. The IRDCs lie close to the Galactic Midplane (Gal. Latitude $b \sim 0^\circ$) where the gas density tend to be higher (Schuller et al. 2009; Rosolowsky et al. 2010; Beuther et al. 2012). As described in Beuther et al. (2012) in more detail the distribution along the Galactic Latitude is symmetric and its peak is close to the Galactic Mid-Plane ($\sim 0.1^\circ$). Therefore observations within a latitude range of $|b| \leq 0.5^\circ$ are recommended to reliably identify IRDCs.

In Fig. 3 the distributions of the sources with detected and non-detected ammonia (1,1)-inversion line have been plotted against the absolute value of their Galactic Latitude b . For both distributions the mean values and medians have been calculated and are marked in Fig. 3. The IRDCs with detected inversion lines (mean: $(0.32 \pm 0.02)^\circ$, median: 0.24°) are significantly closer to the Galactic Mid-Plane than those without (mean: $(0.47 \pm 0.05)^\circ$, median: 0.35°). This implies that identification of IRDCs based on absorption studies against the Galactic background are less

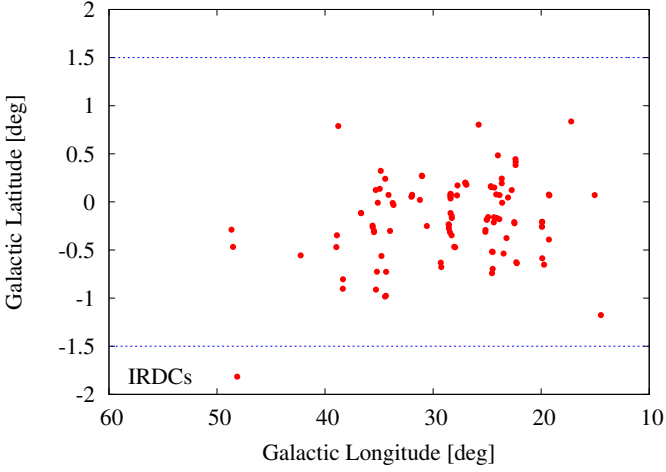


Figure 2: Positions of selected IRDCs with detected ammonia transitions in the Galactic Plane.

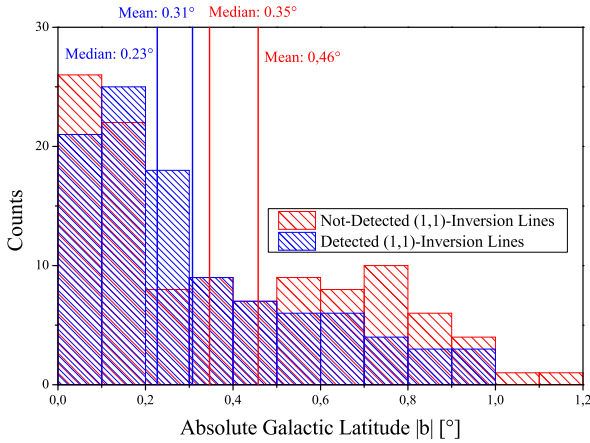


Figure 3: Distribution of IRDCs with detected and without detected ammonia (1,1)-inversion line along the absolute Galactic Latitude.

reliable at larger Galactic Latitudes b .

Schuller et al. (2009) and Beuther et al. (2012) have found a symmetric distribution of compact ATLASGAL sources around the mid-plane of the Milky Way. This is similar to our distribution of the sources where the ammonia (1,1)-inversion transition could be detected. But they have also detected a shift of the distribution peak to $b \sim -0.1^\circ$. However our sample is too small to do a similar analysis.

4.1.3. Distance

In this and the following sections, the results for the physical conditions and virial parameters will be presented and discussed. Therefore, we only take the 109 sources into account which were detected in the ammonia.

To be able to calculate the IRDCs' virial masses, which will be averaged over the beam, we needed the sources' radii. For estimating them, we derived the kinematic distances between the sources and the sun. Using a model for the Galactic rotation with new parameters proposed by Reid et al. (2009), (near and far) kinematic distances of a source with measured LSR velocity at given Galactic coordinates can be derived. The method is de-

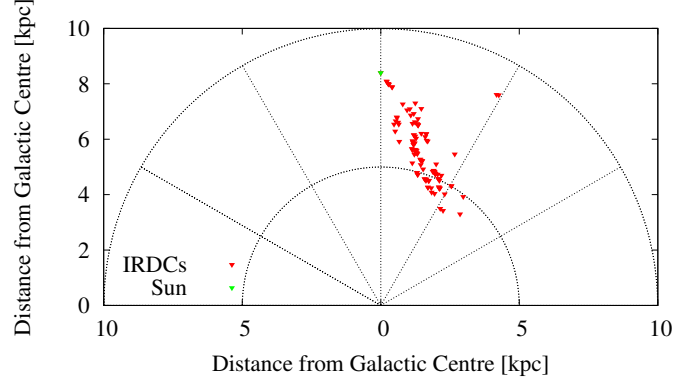


Figure 4: Positions of selected IRDCs within the Galaxy.

scribed in more details in the paper by Reid et al. (2009). Given that the sources in our sample appear in silhouette against background radiation, we chose the near values for sources with a distance ambiguity.

The IRDCs are at distances of a few kilo-parsecs (cf. Table 2 and Table C.2) and have radii between 0.25 pc and 0.5 pc. To estimate these, we assumed the FWHM of the Effelsberg beam ($40''$) as a proxy for the size. Their positions within the Galactic Plane and Galaxy are sketched in the Figs. 2 and 4.

4.2. Rotation and Kinetic Temperature

For deriving the rotation temperatures and column densities, we followed the outlines by Schilke (1989), Ho & Townes (1983) and Ragan et al. (2011). For a better understanding we shortly summarise the most important points in Appendix A.

The calculated results for all sources are presented in Table C.2 in the Appendix. The errors have been derived from Gaussian error propagation. The same applies to all other quantities if not mentioned otherwise.

The statistical properties of the sample are summarised in Table 2 including the mean values and the medians of the derived quantities, as well as the minimal and maximal values.

The IRDCs have rotation temperatures between 8 K and 29 K. Although the latter being an upper limit, the majority of the IRDCs have mean rotation temperatures around 15 K (median: 14 K) being more obvious in Fig. 5. It shows a cumulative distribution of our sample's rotation temperatures (red data points). About 80% of the sources have values between 10 and 20 K. This is consistent with previous studies (Pillai et al. 2006; Peretto et al. 2010; Ragan et al. 2011).

In addition, the blue points show the cumulative distribution of rotation temperatures derived for the sample of 65 high-Mass Protostellar Objects (HMPOs) from Sridharan et al. (2002). This sample had been observed in the same fashion as ours with the Effelsberg telescope. Therefore, the results for rotation temperatures, line width FWHMs and column densities can be compared with the results for our sample IRDCs here. HMPOs are considered to be the next evolutionary step in high-mass star formation after IRDCs (Beuther et al. 2007).

The sample of HMPOs has a mean rotation temperature of 26 K (median: 24 K) which is significantly higher than the value we find for our IRDCs. Therefore, the rotation temperature is a

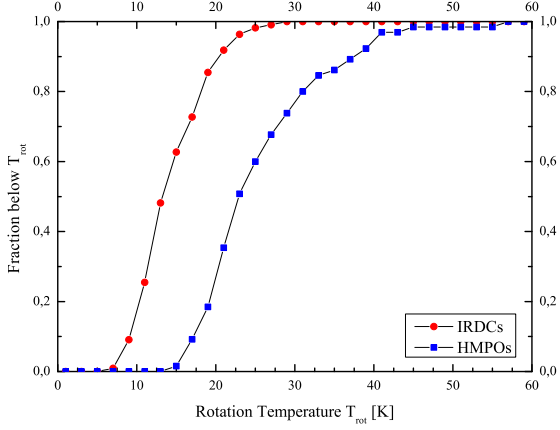


Figure 5: Cumulative distributions of NH_3 rotation temperatures of IRDCs (red data points) and HMPOs (blue data points).

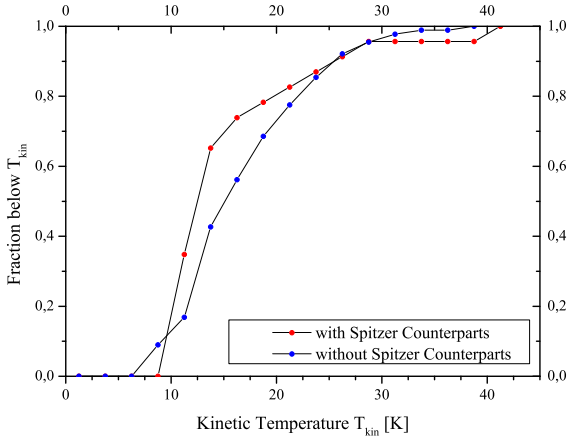


Figure 6: Cumulative distributions based on the sources where NH_3 has been detected. The red subsample includes the sources with Spitzer $24 \mu\text{m}$ association, the blue subsample the ones without.

good indicator for differentiating between evolutionary stages: the rotation temperature increases with evolution. While HMPO temperatures and luminosities mainly stem from internal heating processes (hydrogen burning and accretion), the IRDC temperatures and luminosities are dominated by external radiation fields (Wilcock et al. 2012).

We derived kinetic temperatures with the approximation of Tafalla et al. (2004). More details are given in Appendix A.1. We estimate that they have errors of 5%. The kinetic temperatures of the IRDCs vary between 8 K and 41 K with a mean value of 18 K and a median of 16 K. These values are similar to those of the rotation temperature. This is not surprising, because both quantities are nearly linearly connected until 20 K and, thus, approximately equal within this regime. (Danby et al. 1988). Our results match those of Wienen et al. (2012, median T_{rot} of 17 K) and Dunham et al. (2011, mean T_{kin} of 15.6 K). Furthermore, the trend toward higher rotation temperatures and line widths (cf. Sect. 4.3) with progressing protostellar evolution agrees with the results of Wienen et al. (2012) who compared the relative number and cumulative distributions of different stages between IRDCs and the envelopes of ultracom-

pact HII regions.

Comparing our results with those of Harju et al. (1991, 1993) (mean T_{kin} between 14 and 20 K), our sources have, on average, the same temperature or are slightly cooler. This can be explained by taking into account that Harju et al. included also sources being associated with IRAS sources heating up their envelopes.

Using Spitzer $24 \mu\text{m}$ data we checked for associations with Young Stellar Object (YSO) to identify a sample of starless IRDCs. We looked for any emission source within a circular area of radius $20''$ around the position. The results are listed in the last column of Table C.2. We found that 87 (79.8%) IRDC candidates have no counterpart. But 22 (20.2%) of our sample IRDCs are associated with YSOs or lie close enough to a Spitzer $24 \mu\text{m}$ source that the beam includes parts of them. We also investigated whether there exists a correlation between the (non)detection in Spitzer $24 \mu\text{m}$ and the kinetic temperature. However, no statistically significant difference between the two subsamples could be identify (cf. Fig. 6). This could be explained by considering our beam which covers a greater volume than the still too small and too young protostars are able to influence. While the line widths of sources with and without Spitzer counterparts are almost identical, there is a trend of higher H_2 and NH_3 column densities for sources with Spitzer counterparts. However, since the sample with Spitzer $24 \mu\text{m}$ detections is relatively small (22), it is unclear whether this is statistically significant.

Table 2: Statistics of IRDC sample. The statistics have been built up by the 109 IRDCs with detected ammonia transitions.

IRDC Parameter ^b	Mean	Min.	Median	Max.
T_{rot} [K]	15	8	14	29
T_{kin} [K]	18	8	16	41
N_{NH_3} [10^{14} cm^{-2}]	7.0	0.9	5.1	32.0
$N_{\text{H}_2}^{19''}$ [10^{22} cm^{-2}]	3.5	0.1	2.9	27.3
χ_{NH_3} [10^{-8}]	3.8	0.6	1.9	45.9
Δv_1 [km s^{-1}]	1.7	0.7	1.6	4.0
d [kpc]	3.2	0.4	3.2	5.9
M_{vir}^c [M_{\odot}]	325	6	264	1099
α_{OH}^d	6.1	0.3	2.3	155.2
α_{MRN}^4	1.9	0.1	0.7	49.4

^b Note that T_{rot} represents the rotation temperature, T_{kin} the kinetic temperature, N_{NH_3} the column density of ammonia, $N_{\text{H}_2}^{19''}$ the column density of molecular hydrogen, χ_{NH_3} the abundance of ammonia, Δv_1 the line width FWHM of the ammonia (1,1)-inversion line, d the distance between source and sun, M_{vir} the virial mass and α_i the virial parameters for the used models (cf. Sect. 4.5).

^c The here given virial mass M_{vir} is the mean value of the virial masses for the individual density profiles. Cf. Sect. 4.5.1 for more details.

^d These are the sources' virial parameters, giving the ratio between kinetic and gravitational energy and, thus, an estimation for the stability of the sources. These Parameters will be discussed in more detail in Sect. 4.5.3.

4.3. Line Width

Another observable to characterise IRDCs and HMPOs is the line width. The IRDCs have NH_3 (1,1) line widths of around 1.7 km s^{-1} (mean and median) which agrees with the results of Wienen et al. (2012), but is higher than the values of Harju et al. (1991, 1993). The latter can be explained by taking into account that the sources studied by Harju et al. (1991) are at

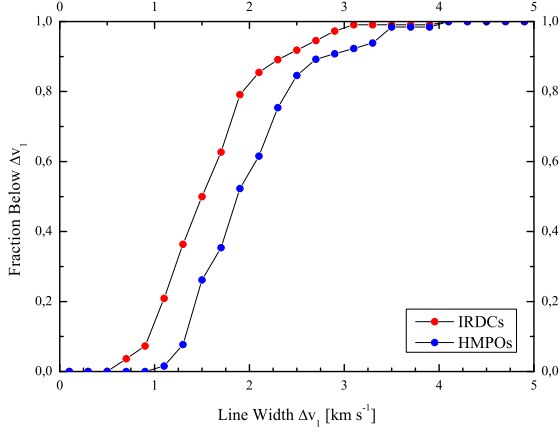


Figure 7: Cumulative distributions of NH_3 line width FWHMs of IRDCs (red data points) and HMPOs (blue data points).

much smaller distances than ours. Thus, for the same beam one sees smaller size scales and hence smaller FWHMs which agrees with the Larson line width - size relation.

We investigated possible correlations between the FWHM and the H_2 column density as well as between the line width and the kinetic temperature. However, no clear correlation between these quantities was found.

Fig. 7 shows that the IRDCs are not only colder than the HMPOs, but have also narrower lines (for HMPOs: mean: 2.1 km s^{-1} , median: 2.0 km s^{-1}). The line widths are larger than expected for thermal emission at the given temperatures ($\approx 0.2 \text{ km s}^{-1}$) observed in low-mass star-forming regions (Kunth et al. 1996). The increased line widths can be caused by intrinsic cloud turbulence, infall motions or outflows from young forming stars.

4.4. Ammonia Column Density

Analogous to the temperatures the derivation of the column density can be found in Appendix A.2. The column densities for the IRDCs are listed up in Table C.2 in the Appendix.

The ammonia column densities range between $9 \cdot 10^{13} \text{ cm}^{-2}$ and $3 \cdot 10^{15} \text{ cm}^{-2}$. The mean value is approximately $7 \cdot 10^{14} \text{ cm}^{-2}$, the median is about $5 \cdot 10^{14} \text{ cm}^{-2}$ (cf. Table 2). As the rotation temperature and the line width, also the column density of ammonia is an observable for the evolution of star-forming regions. Fig. 8 shows that the column densities of our IRDCs are on average smaller than those of the HMPO sample (mean: $4 \cdot 10^{15} \text{ cm}^{-2}$, median: $3 \cdot 10^{15} \text{ cm}^{-2}$). This can be interpreted as evidence that the column densities of ammonia do change on spatial scales traced by single-dish telescopes in these early stages of massive star formation. The ammonia column densities of our sample are about one order of magnitude smaller than the ones of Wienen et al. (2012), but agree with the ones of Harju et al. (1991, 1993) and Dunham et al. (2011). Lower average column densities could be caused by our selection criteria based on absorption shadows. It appears that the extinction features trace the column density peaks less well than the ATLASGAL submm continuum observations.

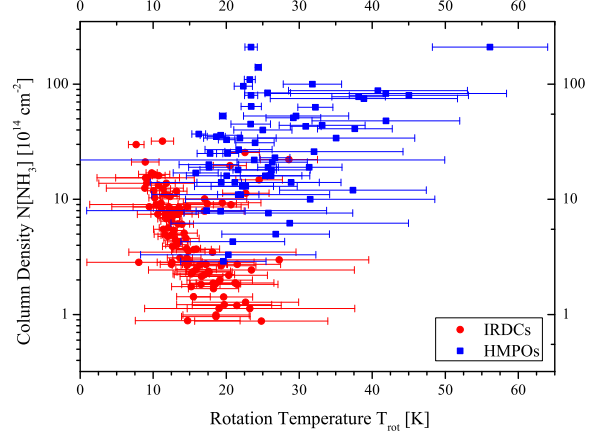


Figure 8: Correlation plot between the NH_3 total column density and the NH_3 rotation temperature of the IRDCs (red data points) and the HMPOs (blue data points).

4.5. Hydrogen Properties and Virial Parameter

4.5.1. Virial Mass

When we derived the virial mass M_{vir} , we only considered the balance between bulk kinetic and gravitational energy. Solving this for the mass and assuming a Gaussian velocity distribution, the virial mass can be calculated by

$$M_{\text{vir}} = k_2 r \Delta v_1^2 \quad (1)$$

where r represents the radius of the source and Δv_1 its FWHM in ammonia (1,1)-inversion transition (MacLaren et al. 1988). k_2 is a constant depending on the assumed density profile (see Table 3).

Table 3: Virial Theorem Coefficient (MacLaren et al. 1988).

Density Distribution	k_2
$\rho \sim r^{-1}$	190
$\rho \sim r^{-2}$	126

It is not clear whether the sources' density profiles follow a r^{-1} - or r^{-2} -power-law. Therefore, the masses $M_{\text{vir}}^{r^{-1}}$ and $M_{\text{vir}}^{r^{-2}}$ were calculated with both power-laws. They are presented in Table C.2. For Table 2 and the further calculations of the virial parameters (cf. Sect. 4.5.3) we used the mean value $M_{\text{vir}} = \frac{1}{2} (M_{\text{vir}}^{r^{-1}} + M_{\text{vir}}^{r^{-2}})$.

The (beam averaged) virial masses range between $6 M_{\odot}$ and $1100 M_{\odot}$ with a mean value of approximately $325 M_{\odot}$ and a median of $264 M_{\odot}$.

4.5.2. Hydrogen Gas Mass

For the calculation of the gas masses, we used the dust emission maps of the ATLASGAL project (Schuller et al. 2009), more precisely the sources' flux densities. For this part we made use of the Gildas GREG package (Buisson et al. 2007). Since the ATLASGAL maps have a HPBW of $19.2''$ we need to smooth them. Otherwise we would not be able to compare them with our Effelsberg data ($40''$ HPBW). We did that by folding the

ATLASGAL maps with a Gaussian of $\sqrt{(40'')^2 - (19'')^2} = 35.1''$. Then, we measured the flux densities F_ν at the locations of the individual IRDC peaks. The errors are estimated to be 20% of the measured flux densities. This is sufficient, because the gas masses' errors are dominated by the error of the dust absorption coefficient. The gas mass M_{gas} is given by

$$M_{\text{gas}} = \frac{d^2 F_\nu^{40''} R}{B_\nu(T_D) \kappa_\nu} \quad (2)$$

where d is the source's distance to the sun, $F_\nu^{40''}$ the total flux density measured in dust emission at $870 \mu\text{m}$ ($\nu = 345 \text{ GHz}$) within the smoothed beam of $40''$. $B_\nu(T_D)$ represents the Planck function for the dust temperature T_D being approximately equal to the kinetic temperature T_{kin} for temperatures below 50 K in the dense environment of IRDCs, since gas and dust temperature are collisionally coupled at high densities in our IRDCs. Furthermore also the kinetic and the rotation temperatures are approximately equal below 50 K. Thus, we inserted the rotation temperature T_{rot} for the dust temperature.

R represents the gas-to-dust mass ratio and κ_ν the dust absorption coefficient. Following Schuller et al. (2009), we assume R to be 100 and $\kappa_{\text{OH}} = 1.85 \text{ cm}^2 \text{ g}^{-1}$ (Schuller et al. 2009; Ossenkopf & Henning 1994). But since these values are just estimated, they contain the biggest uncertainties, particularly the dust absorption coefficient.

In the paper by Ossenkopf & Henning (1994), the dust absorption coefficient dependency on different conditions is described in more detail and the older data of Mathis et al. (1977) are compared with newly derived values. Ossenkopf & Henning list the dust absorption coefficient in dependency of the wavelength and used gas density. The dust absorption coefficient of $\kappa_{\text{OH}} = 1.85 \text{ cm}^2 \text{ g}^{-1}$ was interpolated from Table 1, Col. 5 (Ossenkopf & Henning 1994; Schuller et al. 2009) at a wavelength of $870 \mu\text{m}$. By interpolating the original data of Mathis et al. – given in Table 1, Col. 2 (Ossenkopf & Henning 1994) – we determined the dust absorption coefficient to be $\kappa_{\text{MRN}} = (0.6 \pm 0.1) \text{ cm}^2 \text{ g}^{-1}$. Comparing this with κ_{OH} , this implies an error factor of about 3 in gas mass. Since the exact value is not known, the two models give us an estimate of the upper and lower limits of gas masses (cf. Table 2). We calculated the gas masses for all sample sources with both models, being labelled as M_{OH} and M_{MRN} (as being the corresponding virial parameters).

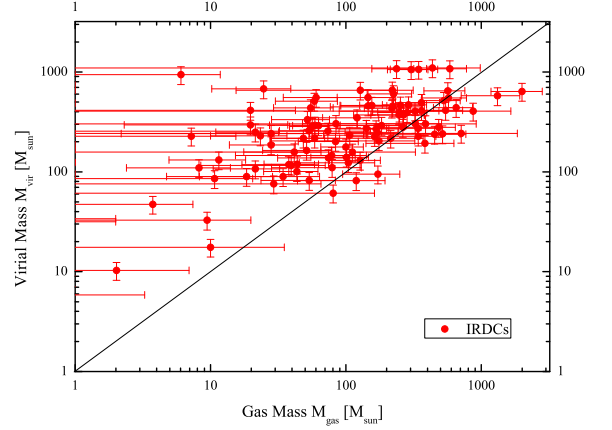
Nevertheless, our sources with masses up to several thousand solar masses are on average more massive than the clumps of Harju et al. (1991, 1993). This is not surprising, because our sample was selected for high-mass cores, while Harju et al. (1991, 1993) observed mainly low- to intermediate-mass cores.

4.5.3. Virial Parameter

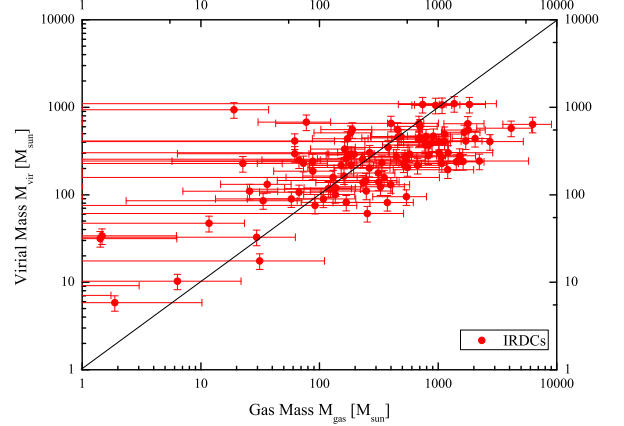
The virial parameter for molecular clouds is defined by

$$\alpha = a \frac{2T}{|W|} = \frac{M_{\text{vir}}}{M_{\text{gas}}} \quad (3)$$

(Bertoldi & McKee 1992) where the dimensionless parameter a is the correction factor for sources having no uniform and spherical mass distribution. T and W represent the kinetic and gravitational energies. Their ratio is equivalent to the ratio of virial and gas mass.



(a) Ossenkopf & Henning (1994): $\kappa_{\text{OH}} = 1.85 \text{ cm}^2 \text{ g}^{-1}$



(b) Mathis et al. (1977): $\kappa_{\text{MRN}} = 0.6 \text{ cm}^2 \text{ g}^{-1}$

Figure 9: Correlation plot between virial and gas mass using the model of Ossenkopf & Henning (1994) and Mathis et al. (1977). The indicated black straight line represents the line of α being equal to 1.

The virial parameter is a helpful tool, because it is an indicator for a source being in virial equilibrium or not. In a simplified picture, a source is in virial equilibrium if its virial parameter is equal to 1. If the virial parameter is bigger than 1, turbulence dominates over gravity and the source expands. Otherwise, if the virial parameter becomes smaller than 1, gravity is the dominating force and the cloud collapses. In reality, additional effects like gas pressure, external pressure and magnetic fields (being ignored in our calculations) influence a cloud's state of equilibrium. Even clouds with $\alpha \gg 1$ can be stable, because these additional terms can change the balance (Bertoldi & McKee 1992).

In Fig. 9 the correlations between the virial and gas masses are plotted for each model. The value $\alpha = 1$ is indicated by a straight black line. For the model of Ossenkopf & Henning (1994) the majority of the IRDCs have virial parameters slightly above 1 (mean: 6, median: 2). In contrast, the majority of the sources' virial parameters in the model of Mathis et al. (1977) are slightly below 1 (mean: 2, median 0.7). Because the models represent maximum and minimum estimates, the real virial parameters are approximately equal to 1 and the sources, thus, are close to virial

equilibrium. This implies that the gas clumps can be stable, but may be at the verge of collapse and star formation.

Our results match those of Dunham et al. (2011), but not quite those of Wielen et al. (2012) and Harju et al. (1993). Wielen et al. (2012) have mean virial parameters of 0.21 for FWHMs smaller than 4 km s^{-1} (and 0.45 for FWHMs larger than 4 km s^{-1} , but we do not have any source with such a large line width) by using the Ossenkopf & Henning model and assuming the equipartition between magnetic and kinetic energy which reduces their value by a factor 0.5. Additionally, the difference is, to some degree, certainly due to their lower spectral resolution of 0.7 km s^{-1} compared to our spectral resolution of 0.38 km s^{-1} , although Wielen et al. corrected for this in their calculation of virial masses. This reduces their used FWHM, and by that the estimate.

In contrast, the virial parameters of Harju et al. (1993) ($= \frac{2 E_{\text{kin}}}{E_{\text{pot}}}$) are between 1.7 and 4 and, therefore, larger than ours.

An explanation could be that their cores are more evolved than ours, indicating a more active phase of star formation. Since their sources can be associated with IRAS sources, this is not surprising. This may look like a contradiction to the small line widths (cf. Sect. 4.3). But considering the smaller solid angles and distances, Harju et al. (1991) observed also smaller absolute values of mass, kinetic and potential energies. Since the virial parameter is calculated by the ratio of kinetic and potential energies, the absolute measured order of magnitude does not really matter, but the relation between the energies. And this relation depends on the evolutionary stage of the objects.

4.5.4. Hydrogen Column Density and Ammonia Abundance

With the ATLASGAL data, we were also able to calculate the column density of molecular hydrogen and the abundance of ammonia compared to hydrogen by using the formula

$$N_{H_2}^{19''} = \frac{F_v^{19''} R}{B_v(T_D) \Omega \kappa_v \mu m_H} \quad (4)$$

(Schuller et al. 2009) where $F_v^{19''}$ is the total flux density measured in dust emission at $870 \mu\text{m}$ within the solid angle of $\Omega = 6.66 \cdot 10^{-9} \text{ sr}$ ($19''$), μ the molecular weight of hydrogen and m_H the weight of one hydrogen atom. For the dust absorption coefficient we adapted $\kappa_v = 1.85 \text{ cm}^2 \text{ g}^{-1}$ from Schuller et al. (2009). The column densities of molecular hydrogen in our sample range between $2 \cdot 10^{20} \text{ cm}^{-2}$ and $3 \cdot 10^{23} \text{ cm}^{-2}$, with an average of $4 \cdot 10^{22} \text{ cm}^{-2}$ and a median of $3 \cdot 10^{22} \text{ cm}^{-2}$ (cf. Table 2). These results match those of Wielen et al. (2012) and Dunham et al. (2011) ($\sim 10^{22} \text{ cm}^{-2}$).

Since the ammonia column densities have been calculated with data observed with a $40''$ beam, we used the smoothed ATLASGAL data for deriving the ammonia abundances $\chi_{NH_3} = N_{NH_3} / N_{H_2}^{40''} \cdot N_{H_2}^{40''}$ is the hydrogen column density derived with Equ. (4) by inserting the total flux density $F_v^{40''}$ within the solid angle $\Omega = 2.95 \cdot 10^{-8} \text{ sr}$ ($40''$, smoothed data which have been also used for calculating the sample sources' gas masses, cf. Sect. 4.5.2). We find NH_3 abundances lie between $6 \cdot 10^{-9}$ and $5 \cdot 10^{-7}$ with a median of $2 \cdot 10^{-8}$. The average abundance is of the order 10^{-8} which agrees with the results of Wielen et al. (2012) and Dunham et al. (2011) ($\sim 5 \cdot 10^{-9} - 5 \cdot 10^{-7}$).

5. Summary and Conclusion

218 candidate IRDCs located between 13° and 50° in Galactic Longitude and $\pm 1.5^\circ$ Galactic Latitude have been observed in the ammonia (1,1)- and (2,2)-inversion transitions with the Effelsberg 100m radio telescope. In 109 sources we found ammonia (1,1)-inversion lines and discussed the physical conditions within them.

We found that there is a correlation between a source's position within the Galactic Plane and the detectability of ammonia. The smaller the absolute value of the source's Galactic Latitude, the greater the chance to find ammonia inversion lines. This makes sense, because ammonia is a high density tracer and the gas density is higher in the inner regions of the Galactic Plane than in the outer ones. To improve the detection rate, future observations should focus on areas of low Galactic Latitudes ($|b| < 0.5^\circ$). The dust emission maps of the ATLASGAL project confirm this statement, because the majority of compact sources detected by them have been found in this area (Beuther et al. 2012). Vice versa, almost all sources with high submm flux densities have counterparts in the IRDC catalogue (Schuller et al. 2009). Therefore, the detection rate could be increased by building up future IRDC samples on the base of the ATLASGAL data. We checked if our sources can be associated with Spitzer $24\mu\text{m}$ emission indicating the existence of Young Stellar Objects embedded within the IRDC candidates. We found the fraction of sample IRDCs having a counterpart in the Spitzer data to be 20.2%, but were not able to find any correlation between the association and the temperatures measured with the ammonia observations.

The observed line widths range between 0.5 and 2.5 km s^{-1} , some up to 4 km s^{-1} , and are much higher than expected for purely thermal broadening ($\approx 0.2 \text{ km s}^{-1}$). Therefore, turbulence has to play an important role to stabilise IRDCs. Additionally, the FWHMs are significantly smaller than the ones of HMPOs, but higher than values measured in low-mass cores. We interpret this as additional evidence for IRDCs representing very early stages of high-mass star formation, although not all of our sample IRDCs will be able to actually form high-mass stars. The rotation temperatures ($8 \leq T_{\text{rot}}/\text{K} \leq 30$) are on average 15 K . Thus, IRDCs are cooler than HMPOs ($\sim 22 \text{ K}$). The ammonia column densities of IRDCs are about an order of magnitude smaller than the ammonia column densities of HMPOs.

Using ATLASGAL data, we computed the gas masses, column densities of molecular hydrogen and ammonia abundance relative to molecular hydrogen. We found molecular hydrogen column densities on the order of 10^{22} cm^{-2} on average implying an average ammonia abundance on the order of 10^{-8} .

The virial masses derived for the cores within the IRDCs are between 100 and a few $1,000 M_\odot$. The corresponding virial parameters are on the order of ~ 1 . Thus, the majority of observed IRDCs is close to virial equilibrium and hence consists of potential candidates for pre-protostellar regions of future star formation.

Acknowledgements. This research has made use of the catalogue of Infrared Dark Clouds and Cores based on MSX data and was built up by Simon et al. as well as the dust emission maps of the ATLASGAL project. L. B. acknowledges support from CONICYT projects FONDAP 15010003 and Basal PFB-06.

References

- Bergin, E. A. & Tafalla, M. 2007, *Ann. Rev. Astron. Astrophys.*, 45, 339
- Bertoldi, F. & McKee, C. F. 1992, *Astrophys. J.*, 395, 140
- Beuther, H., Churchwell, E. B., McKee, C. F., & Tan, J. C. 2007, *Protostars and Planets V*, 165
- Beuther, H., Tackenberg, J., Linz, H., et al. 2012, *Astrophys. J.*, 747, 43
- Buisson, G., Desbats, L., Duvert, G., et al. 2007, *GILDAS GreG Documentation*
- Churchwell, E., Walmsley, C. M., & Cesaroni, R. 1990, *A&AS*, 83, 119
- Danby, G., Flower, D. R., Valiron, P., Schilke, P., & Walmsley, C. M. 1988, *Monthly Notices Roy. Astron. Soc.*, 235, 229
- Dunham, M. K., Rosolowsky, E., Evans, II, N. J., Cyganowski, C., & Urquhart, J. S. 2011, *Astrophys. J.*, 741, 110
- Egan, M. P., Shipman, R. F., Price, S. D., et al. 1998, *ApJ*, 494, L199+
- Harju, J., Walmsley, C. M., & Wouterloot, J. G. A. 1991, *A&A*, 245, 643
- Harju, J., Walmsley, C. M., & Wouterloot, J. G. A. 1993, *A&AS*, 98, 51
- Hily-Blant, P., Pety, J., Guilloteau, S., et al. 2006, *GILDAS CLASS Documentation*, 1.1 edn.
- Ho, P. T. P. & Townes, C. H. 1983, *Ann. Rev. Astron. Astrophys.*, 21, 239
- Kunth, D., Guiderdoni, B., Heydari-Malayeri, M., & Thuan, T. X., eds. 1996, *The interplay between massive star formation, the ISM and galaxy evolution*
- MacLaren, I., Richardson, K. M., & Wolfendale, A. W. 1988, *Astrophys. J.*, 333, 821
- Mathis, J. S., Rumpl, W., & Nordsieck, K. H. 1977, *Astrophys. J.*, 217, 425
- Molinari, S., Brand, J., Cesaroni, R., & Palla, F. 1996, *A&A*, 308, 573
- Ossenkopf, V. & Henning, T. 1994, *A&A*, 291, 943
- Perault, M., Omont, A., Simon, G., et al. 1996, *A&A*, 315, L165
- Peretto, N. & Fuller, G. A. 2009, *A&A*, 505, 405
- Peretto, N., Fuller, G. A., Plume, R., et al. 2010, *A&A*, 518, L98
- Pillai, T., Wyrowski, F., Carey, S. J., & Menten, K. M. 2006, *A&A*, 450, 569
- Ragan, S. E., Bergin, E. A., & Wilner, D. 2011, *Astrophys. J.*, 736, 163
- Reid, M. J., Menten, K. M., Zheng, X. W., et al. 2009, *Astrophys. J.*, 700, 137
- Rosolowsky, E., Dunham, M. K., Ginsburg, A., et al. 2010, *ApJS*, 188, 123
- Schilke, P. 1989, *Master's thesis*
- Schreyer, K., Henning, T., Koempe, C., & Harjunpaeae, P. 1996, *A&A*, 306, 267
- Schuller, F., Menten, K. M., Contreras, Y., et al. 2009, *A&A*, 504, 415
- Simon, R., Jackson, J. M., Rathborne, J. M., & Chambers, E. T. 2006, *Astrophys. J.*, 639, 227
- Sridharan, T. K., Beuther, H., Saito, M., Wyrowski, F., & Schilke, P. 2005, *ApJ*, 634, L57
- Sridharan, T. K., Beuther, H., Schilke, P., Menten, K. M., & Wyrowski, F. 2002, *Astrophys. J.*, 566, 931
- Tafalla, M., Myers, P. C., Caselli, P., & Walmsley, C. M. 2004, *A&A*, 416, 191
- Walmsley, C. M. & Ungerechts, H. 1983, *A&A*, 122, 164
- Wienen, M., Wyrowski, F., Schuller, F., et al. 2012, *A&A*, 544, A146
- Wilcock, L. A., Ward-Thompson, D., Kirk, J. M., et al. 2012, *Monthly Notices Roy. Astron. Soc.*, 424, 716

Appendix A: Derivation of used Formulas

A.1. Rotation and Kinetic Temperature

As described in Sect. 3, the hyperfine fit routine returns the best fit parameters of the brightness temperature, T_{mb} , optical depth, τ , velocity of rest, V_{LSR} , and line width FWHM, Δv , (with errors). The brightness temperature T_{mb} describes the brightness temperature of a source and depends on the beam this source is observed with by returning the mean value over this beam. It is needed to calculate the excitation temperature.

The excitation temperature T_{ex} is no physical temperature, but describes the ratio between two population levels $u(p)$ and $l(o)$ via

$$\frac{n_u}{n_l} = \frac{g_u}{g_l} \exp\left(-\frac{\Delta E}{kT_{\text{ex}}}\right) \quad (\text{A.1})$$

where n_i is the numbers of particles in the state i and g_i its statistical weight. ΔE represents the energy difference between the states and k the Boltzmann constant. For the IRDCs temperatures above 10 K are expected. Thus, (by applying the Rayleigh-Jeans

law) the brightness and excitation temperatures are simplified connected by

$$T_{\text{ex}} = \frac{T_{\text{mb}}}{\eta_f (1 - e^{-\tau})} + T_{\text{BG}} \quad (\text{A.2})$$

with τ being the source's optical depth and T_{BG} the background temperature (being about 2.7 K). η_f represents the beam-filling factor. It describes the fraction of the antenna pattern being received from the source. In the case of extended and not clumpy sources, the beam-filling factor is equal to 1. We assume this case for the sample. The excitation temperatures are calculated for both transition lines.

The rotation temperature T_{rot} is defined similar to the excitation temperature by

$$\frac{n_i^l}{n_j^l} = \frac{g_i}{g_j} \exp\left(-\frac{\Delta E}{kT_{\text{rot}}^{ij}}\right) \quad (\text{A.3})$$

But in contrast to the excitation temperature, the rotation temperature does not describes the ratio between different levels being split by inversion, but between the levels of quantum numbers J and K (total angular momentum and its absolute projection along the z -axis). We are interested in the rotation temperatures of the metastable inversion levels with $J = K$ (non-metastable inversion levels: $J > K$). These levels cannot be populated or depopulated by radiation. Therefore, their population numbers are high enough to emit measurable line intensities. Furthermore, metastable levels interact only via collisions (Ho & Townes 1983; Schilke 1989) and are useful for the calculation of gas temperatures.

The remaining problem is that we do not know the exact population numbers and have to approximate them by the column densities. For lines being observed in the same region the ratio of the population numbers should be equal to the ratio between the corresponding column densities depending on the ratio of the lines' optical depths:

$$\frac{\tau^{JK}}{\tau^{J'K'}} \approx \frac{K^2}{J(J+1)} \frac{J'(J'+1)}{K'^2} \frac{2J'+1}{2J+1} \frac{\Delta v_1}{\Delta v_2} \frac{N_1(J,K)}{N_1(J',K')} \frac{\nu_{JK}}{\nu_{J'K'}} \frac{T_{\text{ex}}^{J'K'}}{T_{\text{ex}}^{JK}} \quad (\text{A.4})$$

where τ^{JK} is the optical depth of the (J,K) -inversion line, Δv_J its line width FWHM, $N_1(J,K)$ its column density and T_{ex}^{JK} its excitation temperature. Because only the $(1,1)$ - and $(2,2)$ -inversion lines have been studied, it is $J = K = 2$ and $J' = K' = 1$ in the following calculations.

Inserting this into Equ. (A.3), one gets:

$$T_{\text{rot}} = -\frac{E}{x \frac{\tau^{JK}}{\tau^{J'K'}}} \quad (\text{A.5})$$

where $E = \frac{h\nu_{ij}}{k} = 41.5$ K (Ho & Townes 1983) and

$$x = \frac{K'^2}{J'(J'+1)} \frac{J(J+1)}{K^2} \frac{2J'+1}{2J+1} \frac{\Delta v_2}{\Delta v_1} \frac{\nu_{J'K'}}{\nu_{JK}} \frac{T_{\text{ex}}^{JK}}{T_{\text{ex}}^{J'K'}} \quad (\text{A.6})$$

Following the instruction of Schilke (1989) and Ho & Townes (1983), there are four cases one has to consider for calculating the rotation temperature. These cases differ in the optical depth of each inversion line:

1. both inversion lines are optical thick:

$$T_{\text{rot}} = -\frac{E}{\ln\left(x \frac{f_1}{f_2} \frac{\tau^{22}}{\tau^{11}}\right)} \quad (\text{A.7})$$

where τ^{ii} is the optical depth of the (i,i)-inversion line and f_i is the relative intensity of the main hyperfine component. For the given transitions, there is $f_1 = 0.5$ and $f_2 = 0.796$ (Ho & Townes 1983).

2. only the (1,1)-inversion line is optical thick and the (2,2)-inversion line is optical thin:

$$T_{\text{rot}} = -\frac{E}{\ln\left[-x \frac{f_1}{\tau^{11} f_2} \ln\left(1 - \frac{\tau^{22}}{\tau^{11}} (1 - e^{-\tau^{11}})\right)\right]} \quad (\text{A.8})$$

3. both inversion lines are optical thin:

$$T_{\text{rot}} = -\frac{E}{\ln\left(-x \frac{f_1}{f_2} \frac{T_{\text{mb}}^1}{T_{\text{mb}}^2}\right)} \quad (\text{A.9})$$

where T_{mb}^i represents the brightness temperature of the (i,i)-inversion line.

4. only the (1,1)-inversion line is detected, the (2,2)-inversion line is not:

$$T_{\text{rot}} = \frac{-E}{\ln\left[-\frac{0.282}{\tau^{11}} \ln\left(1 - \frac{T_{\text{mb}}^2}{T_{\text{mb}}^1} (1 - e^{-\tau^{11}})\right)\right]} \quad (\text{A.10})$$

In this case, the (2,2)-inversion line lies within the noise. To be able to continue with the calculations, T_{mb}^2 has been given the triple value of the average root-mean-square noise (RMS = 0.0925 K). It is important to emphasise that in this case it is not possible to derive exact rotation temperatures, but only upper limit estimations!

Having the rotation temperature of ammonia, we were able to calculate the kinetic temperature of a source's gas by using the approximation of Tafalla et al. (2004):

$$T_{\text{kin}} = \frac{T_{\text{rot}}}{1 - \frac{T_{\text{rot}}}{E} \ln\left[1 + 1.1 \exp\left(-\frac{15.7 \text{ K}}{T_{\text{rot}}}\right)\right]} \quad (\text{A.11})$$

This approximation has been derived with Monte Carlo models and gives an accuracy of 5% in the range between 5 and 20 K. Because the majority of the sample IRDCs are within this range, their errors are set to this.

A.2. Column Density

As mentioned before in Sect. A.1, the column density is related to a source's optical depth (Schilke 1989). If one neglects the background radiation and expresses the excitation temperature in terms of the optical depth, following Schilke (1989), the column density of the (1,1)-inversion level N^{11} can be calculated by

$$N^{11} \approx 2T_{\text{mb}} \frac{\tau}{1 - e^{-f_1 \tau^{11}}} \frac{3h}{8\pi^3} \frac{\sqrt{\pi}}{2\sqrt{\ln(2)}} \frac{J'(J'+1) \Delta v_1}{K'^2} \frac{k}{\mu^2 h\nu_1} \quad (\text{A.12})$$

where $\mu = 1.476$ Debye is the electric dipole moment and $\nu_1 = 23694.496$ MHz the laboratory frequency of the NH_3 (1,1)-inversion transition. To derive the total column density, N_{NH_3} , we assumed that the sources are in thermal equilibrium. In this case, the column density follows a Boltzmann distribution. Additionally, we took into account that Equ. (A.12) calculates the column density of para- NH_3 being the ammonia inversion levels with $K \neq 3n$ (n being an integer) where the hydrogen spins are not parallel. In contrast, the states with parallel

hydrogen spins are called ortho- NH_3 (with $K = 3n$). The statistical weight g_{JK} of ortho- NH_3 is twice the one of para- NH_3 . Therefore, for calculating the total column density of ammonia, one has to take the triple of column density of para- NH_3 (cf. Schilke 1989):

$$N_{\text{NH}_3} = \frac{3 N^{11}}{2(2J' + 1)} \sum_{1,1} g_{11} \exp\left[\left(23.4 \text{ K} - \frac{h\nu_1}{k}\right) \frac{1}{T_{\text{rot}}}\right] \quad (\text{A.13})$$

Appendix B: Position of sample IRDCs within the Galactic Plane

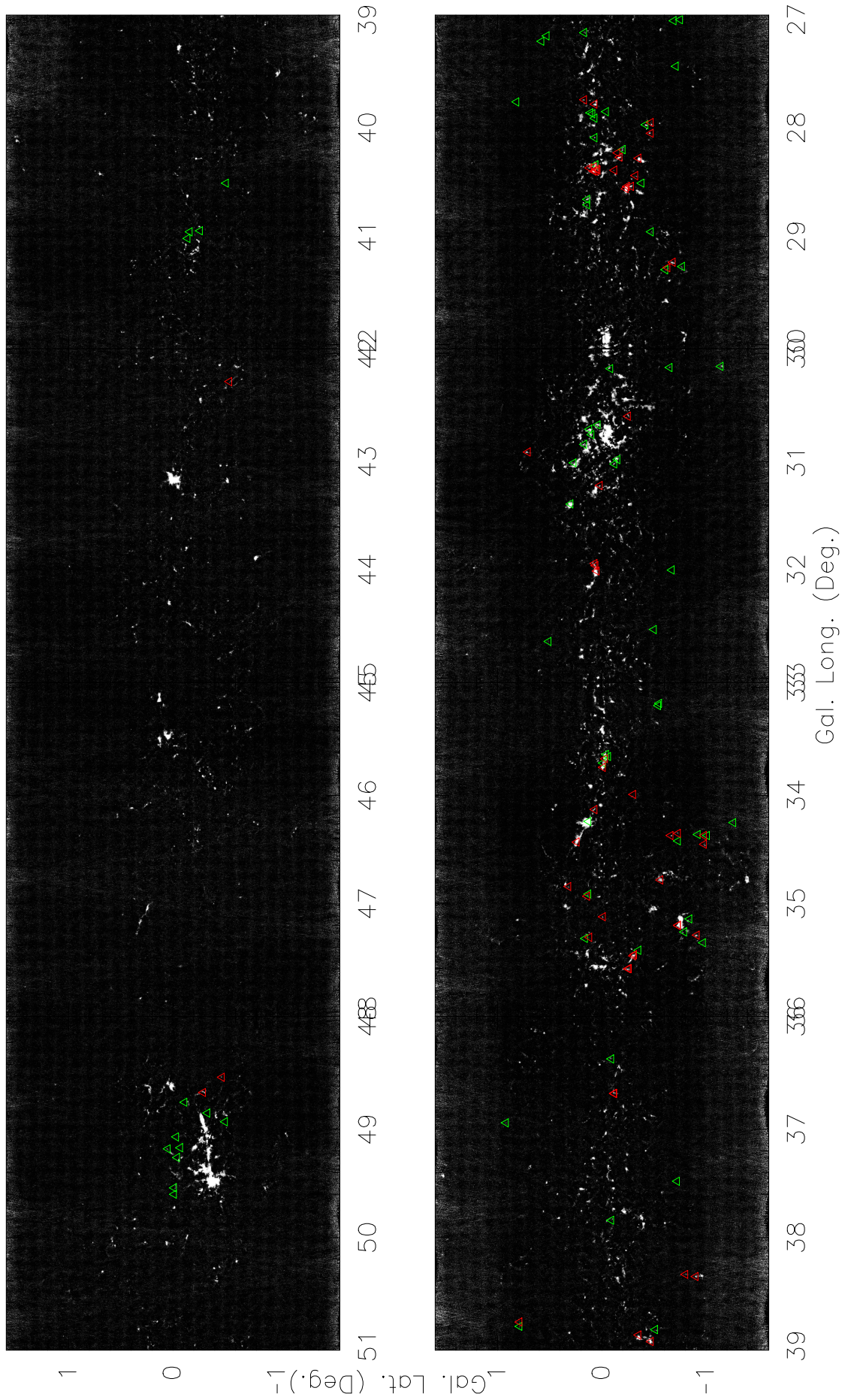


Figure B.1: ATLASGAL dust emission map with indicated sample IRDCs in the range of $l = 27^\circ$ to 51° (Schuller et al. 2009). The red triangles indicate the IRDCs with detected ammonia lines, the green triangles the ones without detected ammonia lines.

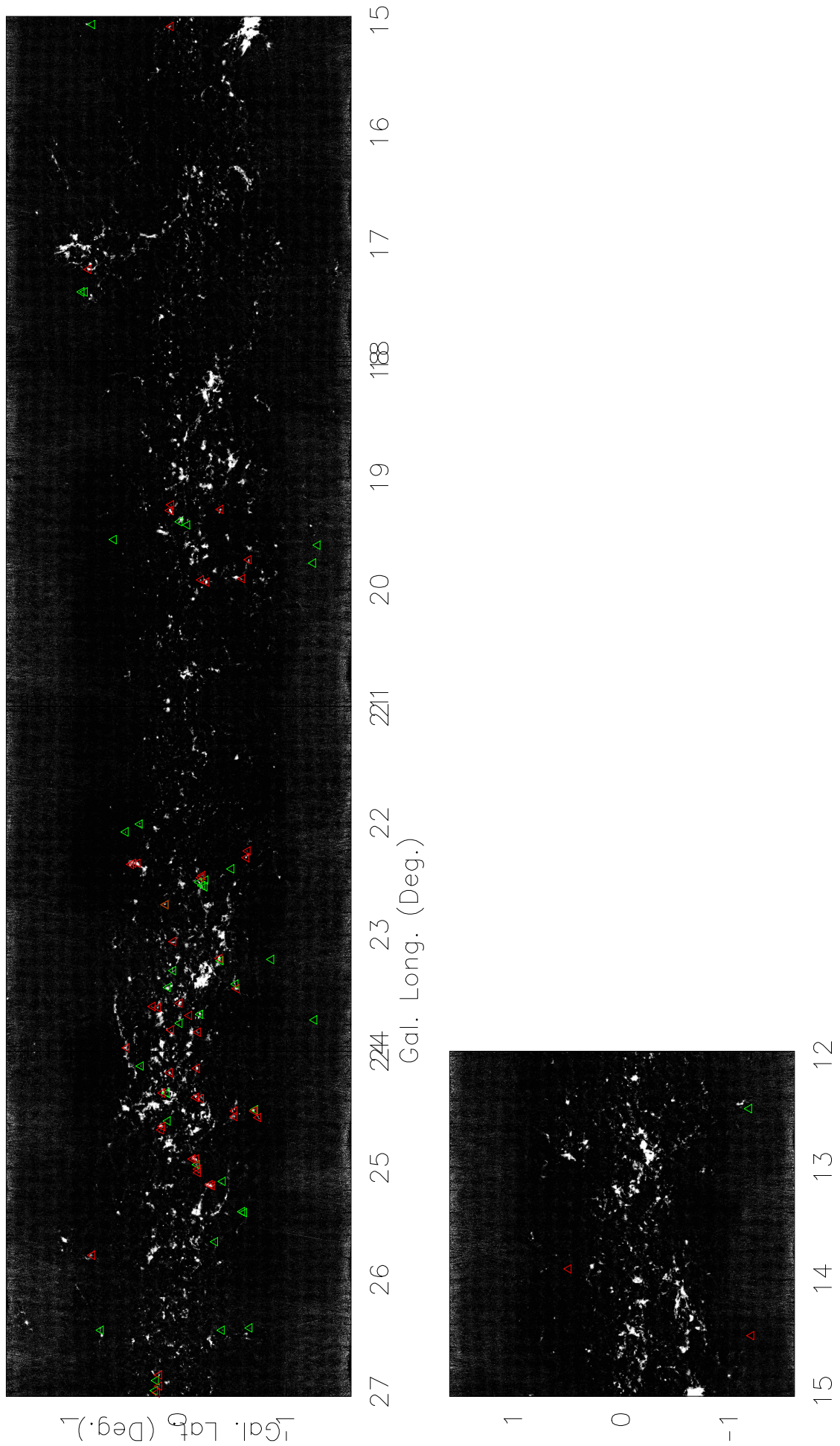


Figure B.2: ATLASGAL dust emission map with indicated sample IRDCs in the range of $l = 12^\circ$ to 27° (Schuller et al. 2009). The red triangles indicate the IRDCs with detected ammonia lines, the green triangles the ones without detected ammonia lines.

Appendix C: Observational and calculated data of sample IRDCs

Table C.1: Coordinates and fit parameters of detected IRDCs in NH_3 . The values of the sources derived with or without detected (2,2)-inversion line are separated by a horizontal line. Note that latter give only upper limits. This table contains the sources' coordinates in Galactic longitude, l , and latitude, b , the brightness temperatures of both transition line, T_{mb}^1 and T_{mb}^2 , the line widths of both lines, Δv_1 and Δv_2 , the LSR velocity of the (1,1)-inversion line, V_{lsr}^1 , and the optical depths of both lines, τ^{11} and τ^{22} .

Source	l	b	T_{mb}^1	\pm	T_{mb}^2	\pm	Δv_1^e	Δv_2^e	V_{lsr}^1	τ^{11}	\pm	τ^{22}	\pm
	deg		K				km s ⁻¹						
G13.90+00.50A	13.90	0.49	2.7	0.4	0.8	0.1	1.5	2.1	22.8	1.83	0.22	0.10	0.21
G15.05+00.07A	15.05	0.07	1.4	0.3	0.3	0.1	1.0	0.8	29.9	2.66	0.29	10.21	4.50
G17.33+00.88A	17.22	0.84	1.8	0.1	0.6	0.0	1.7	2.2	22.5	1.36	0.11	0.10	0.35
G19.27+00.07A	19.29	0.08	2.5	0.2	1.0	0.0	1.8	2.6	26.9	2.24	0.10	0.10	0.10
G19.27+00.07B	19.24	0.07	0.3	0.1	0.3	0.1	4.0	3.7	25.8	1.84	0.57	4.03	1.60
G19.27-00.39A	19.28	-0.39	1.1	0.2	0.3	0.1	1.1	1.4	53.5	1.21	0.34	3.41	1.40
G19.73-00.66A	19.73	-0.65	1.5	0.2	0.3	0.1	1.3	1.6	23.6	1.18	0.21	2.04	1.40
G19.91-00.20A	19.91	-0.21	0.4	0.2	0.3	0.1	2.1	2.3	63.5	2.19	0.62	1.75	1.70
G19.92-00.29A	19.93	-0.26	2.6	0.2	1.2	0.2	3.0	3.3	65.2	2.55	0.15	1.25	0.29
G22.24-00.63A	22.25	-0.64	0.7	0.1	0.3	0.1	1.7	0.7	48.0	1.29	0.38	1.86	2.80
G22.35+00.41A	22.37	0.44	1.1	0.2	0.3	0.1	1.9	1.4	52.7	1.47	0.27	3.89	1.80
G22.35+00.41B	22.36	0.42	0.7	0.1	0.3	0.1	2.2	1.9	84.0	0.19	0.33	0.10	0.39
G22.56-00.20F	22.47	-0.22	1.4	0.2	0.3	0.1	1.2	1.3	75.8	1.45	0.26	0.66	1.80
G22.73+00.11A	22.73	0.12	0.9	0.2	0.3	0.1	1.9	1.6	78.0	1.51	0.38	2.99	1.90
G23.06+00.04A	23.06	0.05	0.8	0.2	0.3	0.1	1.7	3.6	91.3	2.50	0.37	2.90	1.90
G23.22-00.37A	23.21	-0.38	3.1	0.2	2.4	0.5	2.2	2.5	77.7	3.69	0.12	1.59	0.32
G23.42-00.52A	23.48	-0.54	1.0	0.2	0.3	0.1	1.9	1.7	64.2	3.58	0.35	2.71	1.60
G23.60+00.00A	23.61	-0.01	2.0	0.3	0.3	0.1	1.7	1.3	53.6	2.85	0.22	2.86	1.00
G23.71-00.09A	23.72	-0.10	0.8	0.1	0.6	0.0	2.7	3.3	68.7	1.99	0.23	0.10	0.24
G23.71+00.30A	23.64	0.24	1.0	0.3	0.3	0.1	1.2	1.0	110.9	1.77	0.48	5.09	3.50
G23.71+00.30B	23.65	0.19	0.9	0.3	0.3	0.1	1.4	1.3	87.8	0.92	0.56	7.20	3.40
G23.86-00.19A	23.87	-0.18	0.4	0.1	0.3	0.1	1.1	3.9	80.7	1.73	0.64	0.34	2.00
G23.87+00.07A	23.85	0.07	1.0	0.1	0.3	0.1	1.1	1.6	54.1	2.52	0.24	0.72	1.30
G23.99+00.49A	24.01	0.48	1.3	0.2	0.3	0.1	1.4	1.5	94.6	4.30	0.21	3.49	0.59
G24.08+00.04A	24.15	0.08	1.1	0.3	0.3	0.1	1.0	1.0	51.9	4.35	0.36	0.67	1.80
G24.14-00.16A	24.11	-0.17	1.9	0.2	0.8	0.1	1.4	1.4	80.9	2.02	0.16	0.34	0.41
G24.33+00.11B	24.33	0.15	2.5	0.2	1.5	0.2	1.8	2.2	114.2	2.59	0.12	0.89	0.24
G24.36-00.16A	24.37	-0.16	1.2	0.1	0.3	0.1	2.2	1.7	55.9	1.58	0.14	2.82	0.87
G24.37-00.21A	24.38	-0.21	0.7	0.1	0.3	0.1	1.9	2.0	55.3	1.48	0.35	6.55	2.50
G24.49-00.69A	24.49	-0.70	1.7	0.1	0.7	0.2	2.5	2.7	48.4	1.76	0.09	1.04	0.45
G24.54-00.73A	24.55	-0.74	0.7	0.1	0.3	0.1	1.5	2.2	48.6	1.10	0.30	0.15	18.00
G24.55-00.53C	24.54	-0.52	0.6	0.1	0.3	0.1	1.7	0.8	61.1	1.76	0.28	1.35	1.80
G24.60+00.08A	24.63	0.15	2.2	0.2	0.9	0.2	1.8	1.7	53.1	2.09	0.12	1.00	0.39
G25.04-00.20C	25.16	-0.31	1.6	0.1	0.6	0.2	1.9	2.6	63.4	2.25	0.09	0.87	0.54
G25.04-00.20D	25.15	-0.29	2.1	0.1	0.7	0.0	1.5	1.8	63.8	2.12	0.08	0.10	0.33
G25.04-00.20E	24.92	-0.16	2.4	0.1	1.0	0.3	1.5	1.4	47.3	2.31	0.09	1.88	0.46
G25.04-00.20G	24.92	-0.13	1.6	0.1	0.3	0.1	1.8	1.9	48.0	2.01	0.15	1.40	0.63
G25.79+00.81A	25.78	0.80	0.4	0.1	0.3	0.1	2.8	5.0	49.0	2.25	0.43	5.27	2.90
G26.99+00.20A	27.01	0.20	1.1	0.2	0.3	0.1	1.7	1.3	94.1	3.17	0.21	3.40	1.10
G26.99+00.20B	26.95	0.18	0.7	0.2	0.3	0.1	1.4	0.8	92.6	2.01	0.42	4.91	2.70
G26.99+00.20G	26.85	0.18	1.2	0.2	0.3	0.1	1.3	2.9	93.9	2.78	0.27	1.93	0.98
G27.75+00.16A	27.74	0.17	1.1	0.2	0.3	0.1	1.4	1.1	78.2	2.60	0.29	6.41	2.00
G27.84+00.02A	27.78	0.07	1.7	0.1	0.3	0.1	1.6	1.9	101.0	1.52	0.14	1.47	0.93
G27.94-00.47A	27.95	-0.47	0.6	0.1	0.3	0.1	1.3	2.3	45.5	1.44	0.40	9.83	4.30
G28.04-00.46A	28.05	-0.47	1.6	0.2	0.3	0.1	1.4	2.0	45.7	2.37	0.18	0.20	2.60
G28.23-00.19A	28.27	-0.17	1.7	0.2	0.7	0.0	2.1	2.8	79.7	3.55	0.19	0.10	0.07
G28.28-00.34A	28.28	-0.35	2.3	0.2	1.1	0.3	1.5	1.9	48.7	3.55	0.13	0.55	0.45
G28.37+00.07B	28.38	0.05	1.9	0.1	0.3	0.1	2.0	2.2	79.7	2.23	0.12	1.57	0.83
G28.37+00.07C	28.40	0.08	3.7	0.2	2.5	0.4	2.3	3.0	78.1	3.07	0.10	0.64	0.27
G28.37+00.07E	28.39	0.04	1.9	0.2	0.6	0.0	1.8	2.1	79.0	2.24	0.16	0.10	0.35
G28.53-00.25A	28.56	-0.23	2.3	0.5	1.3	0.3	2.8	3.1	86.6	4.90	0.31	1.89	0.29
G28.53-00.25B	28.54	-0.28	2.1	0.2	0.3	0.1	1.3	1.3	88.4	2.30	0.19	2.91	1.10
G28.53-00.25C	28.54	-0.24	1.6	0.2	0.3	0.1	2.0	2.1	86.7	1.50	0.21	0.46	1.30

continued on next page

continued from previous page

Source	l	b	T_{mb}^1	\pm	T_{mb}^2	\pm	Δv_1^e	Δv_2^e	V_{lsr}^1	τ^{11}	\pm	τ^{22}	\pm
	deg		K				km s ⁻¹						
G29.27-00.71A	29.24	-0.68	0.7	0.2	0.3	0.1	1.4	0.9	83.2	2.21	0.48	3.01	3.30
G29.27-00.71B	29.29	-0.63	0.6	0.2	0.3	0.1	1.1	0.8	120.1	0.83	0.54	1.69	3.00
G30.57-00.23A	30.58	-0.25	0.6	0.2	0.1	0.0	1.0	3.0	85.7	1.65	0.51	0.10	0.49
G30.91+00.71A	30.91	0.71	1.3	0.4	0.3	0.1	1.0	1.3	50.8	3.40	0.48	1.69	1.90
G31.22+00.01A	31.22	0.02	1.7	0.2	0.7	0.1	1.6	2.0	75.6	2.32	0.18	0.10	0.28
G31.97+00.07C	31.96	0.06	1.6	0.4	0.3	0.1	2.1	4.3	96.5	1.06	0.47	1.69	2.80
G33.69-00.01A	33.74	-0.01	1.2	0.3	0.3	0.1	1.9	1.9	50.5	3.16	0.36	2.43	0.87
G33.69-00.01B	33.66	-0.03	0.5	0.1	0.3	0.1	2.5	2.5	104.9	1.72	0.46	0.70	1.50
G34.12+00.06A	34.13	0.07	0.8	0.1	0.3	0.1	1.8	1.2	57.0	1.15	0.32	1.58	1.80
G34.37-00.65A	34.37	-0.66	1.9	0.6	0.3	0.1	0.6	0.6	12.3	1.12	0.65	1.43	2.00
G34.43+00.24A	34.43	0.24	1.9	0.2	0.3	0.1	2.2	2.2	57.9	1.31	0.17	0.80	1.00
G34.77-00.55A	34.78	-0.56	2.0	0.1	0.7	0.2	2.0	2.1	41.9	1.45	0.13	0.43	0.59
G34.88+00.29A	34.84	0.32	0.9	0.1	0.3	0.1	1.2	1.5	54.3	1.45	0.26	4.42	2.40
G34.91+00.13A	34.93	0.14	0.6	0.1	0.3	0.1	1.3	5.1	42.2	1.36	0.31	4.83	2.10
G35.19-00.72A	35.20	-0.73	3.7	1.1	1.7	0.3	1.1	1.4	32.6	1.16	0.54	0.54	0.36
G35.28-00.90A	35.29	-0.91	1.4	0.1	0.3	0.1	1.4	1.7	36.7	1.78	0.18	1.29	1.20
G35.33+00.12A	35.31	0.12	0.4	0.0	0.1	0.0	1.5	3.1	13.6	0.10	0.23	0.10	0.99
G35.39-00.33A	35.48	-0.30	3.0	0.3	0.9	0.4	1.4	1.8	45.0	1.92	0.14	1.10	0.64
G35.39-00.33B	35.47	-0.31	2.5	0.3	0.3	0.1	1.1	1.1	45.0	3.06	0.17	1.62	0.91
G35.59-00.24A	35.60	-0.25	1.9	0.3	0.3	0.1	1.2	1.1	44.7	1.78	0.23	0.98	1.80
G35.59-00.24B	35.60	-0.26	0.9	0.1	0.3	0.1	2.4	3.1	43.9	0.20	0.25	4.02	1.50
G36.67-00.11A	36.67	-0.12	1.1	0.2	0.3	0.1	1.3	1.7	53.4	1.34	0.29	2.46	1.50
G38.35-00.90A	38.36	-0.90	3.0	0.2	0.3	0.1	0.9	1.1	16.5	2.20	0.08	0.39	0.86
G42.26-00.54A	42.26	-0.56	0.9	0.1	0.3	0.1	1.5	2.2	72.3	0.95	0.26	10.14	3.90
G48.65-00.29A	48.66	-0.29	1.6	0.2	0.3	0.1	1.2	1.0	33.3	1.61	0.25	14.89	2.60
G79.31+00.36A	79.31	0.36	2.0	0.2	0.3	0.1	0.9	0.9	1.0	3.05	0.18	5.52	1.90
G79.31+00.36B	79.31	0.36	3.0	0.3	0.3	0.1	1.3	1.2	1.7	2.78	0.16	1.55	0.66
G14.49-01.19A	14.50	-1.20	1.9	0.1	0.3	0.1	3.1	0.0	20.8	0.79	0.15	0.00	0.00
G19.89-00.61A	19.90	-0.59	0.5	0.2	0.3	0.1	1.3	0.0	24.1	1.33	0.59	0.00	0.00
G22.29-00.62A	22.31	-0.63	1.2	0.2	0.3	0.1	1.9	0.0	49.1	1.86	0.25	0.00	0.00
G22.35+00.41C	22.36	0.38	1.8	0.2	0.3	0.1	1.8	0.0	84.4	1.63	0.18	0.00	0.00
G22.56-00.20D	22.49	-0.21	1.2	0.2	0.3	0.1	1.5	0.0	75.7	1.16	0.26	0.00	0.00
G24.55-00.53A	24.49	-0.52	0.7	0.1	0.3	0.1	1.4	0.0	61.9	1.24	0.30	0.00	0.00
G24.60+00.08B	24.66	0.16	1.3	0.2	0.3	0.1	1.0	0.0	53.7	2.41	0.19	0.00	0.00
G25.04-00.20B	25.01	-0.18	0.7	0.1	0.3	0.1	1.7	0.0	46.2	0.67	0.27	0.00	0.00
G25.04-00.20F	25.04	-0.18	0.7	0.1	0.3	0.1	1.1	0.0	46.7	1.84	0.28	0.00	0.00
G26.99+00.20E	26.92	0.18	0.9	0.3	0.3	0.1	2.0	0.0	93.7	1.20	0.59	0.00	0.00
G28.23-00.19C	28.28	-0.15	1.1	0.1	0.3	0.1	1.9	0.0	81.1	1.42	0.20	0.00	0.00
G28.37+00.07D	28.36	0.08	1.8	0.2	0.3	0.1	2.2	0.0	80.5	1.71	0.18	0.00	0.00
G28.37+00.07F	28.40	0.06	1.8	0.1	0.3	0.1	1.9	0.0	79.4	2.21	0.13	0.00	0.00
G28.37+00.07G	28.37	0.12	1.4	0.2	0.3	0.1	1.5	0.0	81.6	2.80	0.24	0.00	0.00
G28.38-00.11A	28.39	-0.12	0.5	0.1	0.3	0.1	1.4	0.0	81.5	0.71	0.60	0.00	0.00
G28.53-00.25D	28.44	-0.32	1.0	0.3	0.3	0.1	1.1	0.0	47.2	1.33	0.48	0.00	0.00
G31.97+00.07A	32.01	0.05	1.8	0.3	0.3	0.1	2.6	0.0	40.5	2.04	0.29	0.00	0.00
G31.97+00.07B	31.94	0.07	1.3	0.2	0.3	0.1	2.7	0.0	96.5	1.68	0.26	0.00	0.00
G33.98-00.30A	33.99	-0.30	0.6	0.2	0.3	0.1	0.8	0.0	11.5	1.29	0.72	0.00	0.00
G34.34-00.72A	34.35	-0.73	0.9	0.2	0.3	0.1	0.7	0.0	11.3	1.40	0.36	0.00	0.00
G34.37-00.95C	34.45	-0.98	0.4	0.1	0.3	0.1	1.5	0.0	13.0	1.31	0.60	0.00	0.00
G34.37-00.95D	34.37	-0.98	0.7	0.2	0.3	0.1	0.8	0.0	13.0	1.07	0.55	0.00	0.00
G35.14-00.02A	35.12	-0.01	0.7	0.2	0.3	0.1	0.9	0.0	27.7	2.42	0.52	0.00	0.00
G36.67-00.11A	36.67	-0.12	1.5	0.2	0.3	0.1	1.2	0.0	53.4	2.30	0.21	0.00	0.00
G38.33-00.81A	38.34	-0.80	1.1	0.2	0.3	0.1	0.7	0.0	16.8	3.06	0.33	0.00	0.00
G38.77+00.78A	38.78	0.79	0.6	0.2	0.3	0.1	1.0	0.0	33.6	1.63	0.61	0.00	0.00
G38.92-00.33A	38.90	-0.35	0.7	0.1	0.3	0.1	2.2	0.0	37.9	0.59	0.24	0.00	0.00
G38.95-00.47A	38.96	-0.47	3.0	0.1	0.3	0.1	1.8	0.0	42.2	1.53	0.06	0.00	0.00
G48.52-00.47A	48.52	-0.47	0.5	0.1	0.3	0.1	1.9	0.0	37.9	0.96	0.33	0.00	0.00

^e The errors of Δv_1 , Δv_2 and V_{lsr} are on average smaller than 0.1 km s⁻¹.

Table C.2: Physical Conditions, distances and virial masses of detected IRDCs. The values of the sources derived with or without detected (2,2)-inversion line are separated by a horizontal line. Note that latter give only upper limits. This table contains the sources' ammonia rotation, T_{rot} , and kinetic temperatures, T_{kin} , column densities, N_{NH_3} , distances to the sun, d , and virial masses in dependency of the used density profile, $M_{vir}^{r^{-1}}$ for $\rho \sim r^{-1}$ and $M_{vir}^{r^{-2}}$ for $\rho \sim r^{-2}$. As well it contains a notice about the sources being associated with a Spitzer 24 μm emission sources. "yes" means that there is a Spitzer emission source within the Effelsberg beam at the location given in Table C.1; "no" means that there is not.

Source	T_{rot}	\pm	T_{kin}	N_{NH_3}	d	\pm	$M_{vir}^{r^{-1}}$	\pm	$M_{vir}^{r^{-2}}$	\pm	Spitzer(24 μm)
		K		10^{15} cm^{-2}	kpc		M_{\odot}		M_{\odot}		
G13.90+00.50A	9.2	4.4	9.6	1.5	2.2	0.7	173	57	115	38	no
G15.05+00.07A	12.0	1.3	12.8	0.5	2.6	0.6	98	24	65	16	no
G17.33+00.88A	10.4	9.1	11.0	0.9	1.8	0.7	190	74	126	49	no
G19.27+00.07A	8.9	1.9	9.2	2.1	2.0	0.7	246	82	163	55	no
G19.27+00.07B	27.3	12.2	38.1	0.3	1.9	0.7	1129	406	749	269	no
G19.27-00.39A	14.7	2.0	16.3	0.3	3.5	0.5	157	23	104	15	yes
G19.73-00.66A	13.5	1.5	14.8	0.4	1.7	0.7	108	44	71	29	yes
G19.91-00.20A	20.3	5.3	24.9	0.2	3.8	0.4	612	87	406	58	no
G19.92-00.29A	20.5	2.3	25.1	2.0	3.9	0.4	1270	136	842	90	yes
G22.24-00.63A	17.6	3.2	20.6	0.2	3.0	0.5	301	56	199	37	no
G22.35+00.41A	14.2	1.8	15.8	0.5	3.2	0.5	446	72	296	48	no
G22.35+00.41B	23.5	14.1	30.4	0.2	4.5	0.4	789	95	523	63	no
G22.56-00.20F	13.2	1.5	14.4	0.4	4.2	0.4	213	24	141	16	no
G22.73+00.11A	15.6	2.4	17.6	0.4	4.2	0.4	550	67	365	44	no
G23.06+00.04A	14.8	2.3	16.5	0.4	4.7	0.4	476	45	316	30	no
G23.22-00.37A	28.6	3.9	41.2	2.2	4.2	0.4	780	78	517	52	yes
G23.42-00.52A	12.3	1.5	13.2	0.8	3.6	0.5	472	61	313	40	no
G23.60+00.00A	10.7	1.0	11.3	1.3	3.2	0.5	328	53	217	35	yes
G23.71-00.09A	9.5	5.1	9.9	0.9	3.8	0.4	1028	125	682	83	no
G23.71+00.30A	14.5	2.2	16.1	0.3	5.4	0.4	279	31	185	21	no
G23.71+00.30B	17.0	4.1	19.6	0.2	4.5	0.4	328	51	217	34	no
G23.86-00.19A	24.8	9.1	33.0	0.1	4.3	0.4	190	29	126	19	no
G23.87+00.07A	13.7	1.7	15.0	0.3	3.2	0.5	143	23	95	15	no
G23.99+00.49A	11.1	1.1	11.8	0.8	4.8	0.4	335	29	222	19	no
G24.08+00.04A	11.4	1.3	12.1	0.6	3.0	0.5	114	20	76	13	no
G24.14-00.16A	12.0	4.2	12.9	0.7	4.3	0.4	286	29	190	19	no
G24.33+00.11B	22.7	3.2	28.9	1.1	5.5	0.4	623	49	413	32	yes
G24.36-00.16A	13.9	1.6	15.3	0.6	3.2	0.5	557	87	369	58	no
G24.37-00.21A	17.2	2.9	20.0	0.3	3.2	0.5	401	68	266	45	no
G24.49-00.69A	19.4	5.3	23.4	0.9	2.8	0.5	666	125	441	83	yes
G24.54-00.73A	18.5	3.5	21.9	0.2	2.8	0.5	224	44	148	29	no
G24.55-00.53C	17.6	3.0	20.5	0.2	3.4	0.5	366	55	242	36	no
G24.60+00.08A	17.4	4.0	20.2	0.9	3.1	0.5	350	59	232	39	no
G25.04-00.20C	13.9	3.4	15.2	0.8	3.5	0.5	446	61	296	41	no
G25.04-00.20D	9.1	6.5	9.4	1.4	3.5	0.5	292	40	194	26	no
G25.04-00.20E	20.6	2.4	25.4	0.9	2.8	0.5	242	47	160	31	no
G25.04-00.20G	12.3	1.2	13.2	0.8	2.8	0.5	324	62	215	41	no
G25.79+00.81A	21.5	5.9	26.9	0.3	2.8	0.5	814	161	540	107	no
G26.99+00.20A	12.3	1.3	13.2	0.7	4.7	0.5	493	50	327	33	yes
G26.99+00.20B	16.6	2.9	19.1	0.2	4.6	0.5	310	38	206	25	no
G26.99+00.20G	12.5	1.4	13.5	0.5	4.7	0.5	273	28	181	19	yes
G27.75+00.16A	13.1	1.6	14.2	0.4	4.0	0.5	271	34	179	22	yes
G27.84+00.02A	12.5	1.3	13.5	0.7	4.9	0.5	496	51	329	34	no
G27.94-00.47A	18.2	3.4	21.5	0.2	2.5	0.6	158	37	105	25	no
G28.04-00.46A	11.8	1.2	12.7	0.7	2.5	0.6	197	45	131	30	no
G28.23-00.19A	7.7	1.1	7.8	3.0	4.1	0.5	694	85	460	56	no
G28.28-00.34A	10.1	2.1	10.6	1.7	2.7	0.6	232	49	154	32	yes
G28.37+00.07B	11.4	1.0	12.1	1.2	4.1	0.5	595	73	394	48	no
G28.37+00.07C	11.3	1.5	12.0	3.2	4.0	0.5	768	95	509	63	yes
G28.37+00.07E	9.0	6.7	9.3	1.5	4.0	0.5	488	61	324	40	no
G28.53-00.25A	22.6	2.0	28.7	2.5	4.4	0.5	1294	149	858	99	no
G28.53-00.25B	11.1	1.0	11.7	0.9	4.4	0.5	289	33	191	22	no
G28.53-00.25C	12.9	1.4	14.0	0.8	4.4	0.5	662	79	439	52	no

continued on next page

continued from previous page

Source	T_{rot}	\pm	T_{kin}	N_{NH_3}	d	\pm	M_{vir}^{r-1}	\pm	M_{vir}^{r-2}	\pm	Spitzer(24 μ m)
		K		10^{15} cm^{-2}	kpc		M_{\odot}		M_{\odot}		
G29.27-00.71A	15.9	2.8	18.0	0.2	4.2	0.5	299	43	198	29	no
G29.27-00.71B	19.7	6.5	23.9	0.1	5.8	0.1	261	29	173	19	no
G30.57-00.23A	8.0	7.1	8.2	0.3	4.3	0.5	168	26	112	17	no
G30.91+00.71A	11.6	1.5	12.4	0.5	2.7	0.6	96	22	64	14	no
G31.22+00.01A	8.9	5.3	9.2	1.2	3.9	0.6	364	53	241	35	yes
G31.97+00.07C	13.3	2.0	14.5	0.7	4.8	0.6	790	142	524	94	no
G33.69-00.01A	12.1	1.5	13.1	0.8	2.6	0.6	366	88	242	59	no
G33.69-00.01B	19.5	4.3	23.5	0.3	5.4	0.1	1277	122	847	81	no
G34.12+00.06A	17.2	2.9	19.9	0.3	3.0	0.6	352	78	234	52	no
G34.37-00.65A	12.6	2.0	13.6	0.3	0.4	0.8	7	19	4	12	yes
G34.43+00.24A	12.3	1.2	13.3	1.1	3.0	0.6	559	119	371	79	no
G34.77-00.55A	14.7	7.4	16.3	0.9	2.2	0.7	306	95	203	63	no
G34.88+00.29A	15.4	2.2	17.4	0.2	2.8	0.6	142	33	94	22	yes
G34.91+00.13A	19.7	3.9	23.7	0.1	2.2	0.7	132	41	87	27	no
G35.19-00.72A	17.0	5.5	19.6	0.8	1.6	0.7	74	32	49	21	yes
G35.28-00.90A	12.8	1.4	13.9	0.5	1.9	0.7	139	51	92	34	no
G35.33+00.12A	14.7	7.2	16.4	0.1	0.5	0.8	41	64	27	43	no
G35.39-00.33A	17.1	5.7	19.7	1.0	2.3	0.7	175	51	116	34	no
G35.39-00.33B	10.0	0.8	10.5	1.2	2.3	0.7	98	28	65	19	no
G35.59-00.24A	11.8	1.2	12.6	0.7	2.3	0.7	133	39	88	26	no
G35.59-00.24B	18.1	11.5	21.3	0.3	2.3	0.7	496	150	329	100	yes
G36.67-00.11A	14.6	1.9	16.3	0.3	2.7	0.7	166	42	110	28	no
G38.35-00.90A	10.2	0.8	10.7	1.0	0.6	0.8	21	26	14	17	yes
G42.26-00.54A	16.4	2.6	18.7	0.3	4.0	0.0	342	16	227	11	no
G48.65-00.29A	12.6	1.4	13.7	0.5	1.7	1.0	91	55	60	36	no
G79.31+00.36A	10.6	0.9	11.2	0.7	4.3	0.4	132	11	88	7	yes
G79.31+00.36B	9.8	0.8	10.2	1.7	4.3	0.4	261	23	173	15	yes
G14.49-01.19A	13.2	1.4	14.4	1.2	1.9	0.7	681	265	451	175	no
G19.89-00.61A	21.4	6.1	26.7	0.1	1.7	0.7	103	42	68	28	no
G22.29-00.62A	13.4	1.6	14.7	0.6	3.0	0.5	418	73	277	48	no
G22.35+00.41C	12.2	1.2	13.1	0.9	4.5	0.4	529	48	351	32	no
G22.56-00.20D	14.6	1.9	16.2	0.4	4.1	0.4	348	38	231	25	no
G24.55-00.53A	18.2	3.2	21.4	0.2	3.5	0.5	261	38	173	25	no
G24.60+00.08B	12.6	1.4	13.7	0.4	3.1	0.5	121	20	80	13	no
G25.04-00.20B	19.1	4.5	22.9	0.2	2.7	0.5	275	58	183	38	no
G25.04-00.20F	16.5	2.6	18.9	0.2	2.7	0.5	129	26	85	17	no
G26.99+00.20E	15.9	3.2	18.0	0.4	4.7	0.5	667	130	442	86	no
G28.23-00.19C	14.5	1.8	16.1	0.5	4.1	0.5	521	65	346	43	no
G28.37+00.07D	12.1	1.2	13.0	1.1	4.1	0.5	726	90	482	60	no
G28.37+00.07F	11.6	1.1	12.3	1.1	4.1	0.5	563	69	374	46	yes
G28.37+00.07G	11.8	1.2	12.6	0.7	4.2	0.5	335	41	222	27	no
G28.38-00.11A	23.2	14.4	29.9	0.1	4.1	0.5	291	47	193	31	no
G28.53-00.25D	15.2	2.5	17.1	0.2	2.6	0.6	108	26	72	17	no
G31.97+00.07A	11.8	1.2	12.6	1.4	2.2	0.6	538	161	357	107	no
G31.97+00.07B	13.5	1.6	14.8	0.8	4.8	0.6	1322	185	877	122	no
G33.98-00.30A	18.6	4.7	22.0	0.1	0.4	0.8	9	18	6	12	no
G34.34-00.72A	15.5	2.3	17.5	0.1	0.4	0.8	7	16	5	10	no
G34.37-00.95C	22.6	7.3	28.9	0.1	0.5	0.8	38	64	25	42	no
G34.37-00.95D	18.6	4.5	22.1	0.1	0.5	0.8	11	19	7	12	no
G35.14-00.02A	15.2	2.7	17.1	0.2	1.4	0.7	39	21	26	14	no
G36.67-00.11A	12.1	1.2	12.9	0.6	2.8	0.7	148	37	98	25	no
G38.33-00.81A	12.5	1.5	13.5	0.3	0.7	0.8	12	15	8	10	no
G38.77+00.78A	19.0	4.3	22.7	0.1	1.7	0.7	57	26	38	17	no
G38.92-00.33A	19.3	4.7	23.2	0.3	1.9	0.7	354	139	235	92	no
G38.95-00.47A	10.8	0.9	11.4	1.6	2.1	0.7	261	90	173	60	yes
G48.52-00.47A	21.5	5.6	26.9	0.2	2.0	1.0	274	145	181	96	no

Table C.3: Studies based on ATLASGAL data of detected IRDCs. The values of the sources derived with or without detected (2,2)-inversion line are separated by a horizontal line. Note that latter give only upper limits. The table contains the sources' flux density, $F_v^{19''} / F_v^{40''}$, in dust emission at $870 \mu\text{m}$ within a $19'' / 40''$ beam, hydrogen column density, $N_{H_2}^{19''} / N_{H_2}^{40''}$, ammonia abundance within a $40''$ beam by using $\kappa_{OH} = 1.85 \text{ cm}^2 \text{ g}^{-1}$, χ_{NH_3} , gas masses, M_{OH} by using the Ossenkopf & Henning model and M_{MRN} by using the Mathis et al. model, and virial parameters, α_{OH} by using the Ossenkopf & Henning model and α_{MRN} by using the Mathis et al. model.

Source	$F_v^{19''}$	$F_v^{40''}$	$N_{H_2}^{19''}$	$N_{H_2}^{40''}$	χ_{NH_3}	M_{OH}	\pm	M_{MRN}	\pm	α_{OH}	\pm	α_{MRN}	\pm
	Jy		10^{22} cm^{-2}		10^{-8}		M_{\odot}			$\kappa_{OH} = 1.85 \text{ cm}^2 \text{ g}^{-1}$		$\kappa_{MRN} = 0.59 \text{ cm}^2 \text{ g}^{-1}$	
G15.05+00.07A	0.12	0.64	1.0	1.3	3.8	54	30	168	98	1.5	0.9	0.5	0.3
G17.33+00.88A	0.31	2.01	3.1	4.6	2.0	112	214	350	676	1.4	2.7	0.5	0.9
G19.27-00.39A	0.42	1.19	3.0	1.9	1.4	127	52	400	175	1.0	0.5	0.3	0.2
G19.27+00.07A	0.56	1.95	6.7	5.3	4.0	175	147	551	471	1.2	1.0	0.4	0.3
G19.27+00.07B	0.31	0.47	1.2	0.4	7.5	6	6	19	18	155.2	150.5	49.4	48.6
G19.73-00.66A	0.41	1.15	3.2	2.0	2.1	34	30	108	94	2.6	2.3	0.8	0.7
G19.91-00.20A	0.29	0.74	1.4	0.8	2.3	55	26	172	85	8.0	4.1	2.5	1.4
G19.92-00.29A	0.98	3.74	4.1	3.5	4.2	236	81	741	279	4.6	1.8	1.5	0.6
G22.24-00.63A	0.15	0.37	0.9	0.5	4.8	21	10	67	34	11.7	6.2	3.7	2.1
G22.35+00.41A	1.06	2.79	7.8	4.6	1.1	266	113	835	380	1.4	0.7	0.4	0.2
G22.35+00.41B	0.42	1.46	1.8	1.4	1.7	128	112	400	358	5.1	4.6	1.6	1.5
G22.56-00.20F	0.27	0.54	2.1	1.0	4.2	100	35	313	119	1.8	0.7	0.6	0.2
G22.73+00.11A	0.24	1.01	1.6	1.5	2.4	146	54	458	186	3.1	1.3	1.0	0.5
G23.06+00.04A	0.36	1.28	2.6	2.0	1.8	248	90	778	309	1.6	0.7	0.5	0.2
G23.22-00.37A	3.41	9.65	12.2	7.8	2.8	566	189	1776	658	1.1	0.4	0.4	0.2
G23.42-00.52A	0.55	1.78	4.7	3.4	2.2	283	112	889	378	1.4	0.6	0.4	0.2
G23.60+00.00A	0.61	2.17	6.1	4.9	2.7	341	141	1071	475	0.8	0.4	0.3	0.1
G23.71+00.30A	0.10	0.41	0.7	0.7	4.3	107	38	335	132	2.2	0.9	0.7	0.3
G23.71+00.30B	0.34	0.98	2.1	1.3	1.6	142	66	444	218	1.9	1.0	0.6	0.3
G23.86-00.19A	0.19	0.56	0.8	0.5	1.7	41	24	130	78	3.8	2.3	1.2	0.8
G23.87+00.07A	0.29	0.43	2.2	0.8	4.1	44	19	137	63	2.7	1.3	0.9	0.4
G23.99+00.49A	0.34	1.45	3.2	3.1	2.7	484	157	1520	548	0.6	0.2	0.2	0.1
G24.08+00.04A	0.42	1.33	3.9	2.8	2.0	172	78	540	259	0.6	0.3	0.2	0.1
G24.14-00.16A	0.52	1.96	4.6	3.9	1.9	452	317	1419	1021	0.5	0.4	0.2	0.1
G24.33+00.11B	0.84	3.86	3.8	4.0	2.9	528	169	1658	592	1.0	0.4	0.3	0.1
G24.36-00.16A	0.39	1.54	2.9	2.6	2.3	155	65	488	218	3.0	1.4	0.9	0.5
G24.37-00.21A	0.27	0.74	1.6	1.0	2.7	52	24	163	79	6.4	3.2	2.0	1.1
G24.49-00.69A	0.99	3.13	5.3	3.8	2.5	145	85	457	277	3.8	2.4	1.2	0.8
G24.54-00.73A	0.13	0.56	0.7	0.7	2.6	28	14	88	47	6.7	3.6	2.1	1.2
G24.55-00.53C	0.34	1.07	2.0	1.4	1.7	85	37	265	123	3.6	1.7	1.1	0.6
G24.60+00.08A	0.95	2.86	5.7	3.9	2.4	183	96	575	316	1.6	0.9	0.5	0.3
G25.04-00.20C	0.65	2.04	4.9	3.5	2.3	247	133	775	434	1.5	0.9	0.5	0.3
G25.04-00.20D	0.77	2.59	9.0	6.9	2.0	709	1132	2225	3571	0.3	0.6	0.1	0.2
G25.04-00.20E	0.85	2.08	4.2	2.3	3.8	84	39	263	131	2.4	1.2	0.8	0.4
G25.04-00.20G	0.51	1.74	4.3	3.4	2.3	167	78	525	260	1.6	0.8	0.5	0.3
G25.79+00.81A	0.20	0.63	0.9	0.7	4.0	25	14	77	47	27.5	17.0	8.8	5.6
G26.99+00.20A	0.52	1.35	4.4	2.6	2.7	361	125	1133	430	1.1	0.5	0.4	0.2
G26.99+00.20B	0.11	0.34	0.7	0.5	4.4	53	21	168	72	4.8	2.2	1.5	0.7
G26.99+00.20G	0.60	1.33	5.1	2.5	1.9	342	119	1075	411	0.7	0.3	0.2	0.1
G27.75+00.16A	0.42	0.92	3.4	1.7	2.6	163	62	512	211	1.4	0.6	0.4	0.2
G27.84+00.02A	0.52	1.89	4.4	3.6	2.0	545	183	1711	635	0.8	0.3	0.2	0.1
G27.94-00.47A	0.00	0.28	0.0	0.4	4.6	12	7	36	22	11.4	6.9	3.6	2.3
G28.04-00.46A	0.13	0.61	1.1	1.2	6.0	51	27	161	89	3.2	1.8	1.0	0.6
G28.23-00.19A	0.93	2.42	13.1	7.7	3.9	1316	606	4130	2011	0.4	0.2	0.1	0.1
G28.28-00.34A	0.82	3.01	8.6	7.1	2.3	384	243	1204	786	0.5	0.3	0.2	0.1
G28.37+00.07B	0.50	1.54	4.7	3.2	3.8	361	129	1134	444	1.4	0.6	0.4	0.2
G28.37+00.07C	2.91	8.69	27.3	18.4	1.7	1998	818	6271	2754	0.3	0.1	0.1	0.0
G28.37+00.07E	0.41	0.86	4.9	2.3	6.6	324	538	1016	1695	1.3	2.1	0.4	0.7
G28.53-00.25A	1.92	6.67	8.8	6.9	3.7	586	192	1839	669	1.8	0.7	0.6	0.2
G28.53-00.25B	0.62	1.78	5.9	3.8	2.4	517	180	1623	620	0.5	0.2	0.1	0.1
G28.53-00.25C	0.79	2.69	6.5	4.9	1.6	571	205	1794	703	1.0	0.4	0.3	0.1
G29.27-00.71A	0.28	1.23	1.8	1.8	1.4	170	72	535	241	1.5	0.7	0.5	0.2
G29.27-00.71B	0.15	0.31	0.8	0.4	3.4	59	31	185	102	3.7	2.1	1.2	0.7

continued from previous page

continued from previous page

Source	$F_v^{19''}$	$F_v^{40''}$	$N_{H_2}^{19''}$	$N_{H_2}^{40''}$	χ_{NH_3}	M_{OH}	\pm	M_{MRN}	\pm	α_{OH}	\pm	α_{MRN}	\pm
	Jy		10^{22} cm^{-2}		10^{-8}			M_\odot		$\kappa_{OH} = 1.85 \text{ cm}^2 \text{ g}^{-1}$		$\kappa_{MRN} = 0.59 \text{ cm}^2 \text{ g}^{-1}$	
G30.57-00.23A	0.28	0.91	3.8	2.8	1.0	498	1056	1563	3325	0.3	0.6	0.1	0.2
G31.97+00.07A	0.84	3.61	9.9	9.6	2.0	370	1444	1160	4537	1.2	4.7	0.4	1.5
G31.97+00.07C	0.39	0.90	3.1	1.6	4.7	220	94	689	315	3.0	1.4	1.0	0.5
G33.69-00.01A	0.84	3.76	7.3	7.4	1.1	325	183	1019	596	0.9	0.6	0.3	0.2
G33.69-00.01B	0.49	2.09	2.6	2.5	1.1	344	131	1080	446	3.1	1.3	1.0	0.5
G34.12+00.06A	0.26	0.98	1.6	1.3	2.1	59	32	185	104	5.0	2.9	1.6	0.9
G34.43+00.24A	0.56	2.32	4.8	4.5	2.4	252	126	792	416	1.8	1.0	0.6	0.3
G34.77-00.55A	0.39	1.75	2.8	2.8	3.0	74	78	231	248	3.5	3.7	1.1	1.2
G34.88+00.29A	0.25	0.58	1.7	0.9	2.7	38	21	119	68	3.1	1.8	1.0	0.6
G34.91+00.13A	0.08	0.30	0.4	0.4	3.9	8	6	26	19	13.4	9.9	4.3	3.2
G35.19-00.72A	1.54	4.52	9.4	6.2	1.3	87	88	272	278	0.7	0.7	0.2	0.2
G35.28-00.90A	0.53	0.99	4.3	1.8	2.9	39	31	123	99	2.9	2.4	0.9	0.8
G35.39-00.33A	0.64	2.07	3.9	2.8	3.5	78	63	246	202	1.9	1.5	0.6	0.5
G35.39-00.33B	0.32	1.23	3.4	2.9	4.1	119	75	373	243	0.7	0.5	0.2	0.1
G35.59-00.24A	0.35	1.13	3.1	2.3	3.0	79	51	248	164	1.4	0.9	0.4	0.3
G35.59-00.24B	0.15	0.60	0.9	0.8	4.5	20	23	62	72	21.0	24.5	6.7	7.9
G36.67-00.11A	0.39	1.09	2.8	1.8	1.8	74	43	233	140	1.9	1.1	0.6	0.4
G38.35-00.90A	0.34	1.37	3.6	3.2	3.2	10	25	31	79	1.8	4.4	0.6	1.4
G42.26-00.54A	0.24	0.48	1.5	0.7	3.9	56	18	177	63	5.1	1.9	1.6	0.7
G48.65-00.29A	0.27	0.92	2.2	1.7	2.9	29	36	92	115	2.6	3.2	0.8	1.0
G19.89-00.61A	0.22	0.72	1.0	0.8	1.5	11	10	34	31	8.0	7.5	2.5	2.4
G22.29-00.62A	0.47	1.28	3.7	2.3	2.7	121	54	380	179	2.9	1.4	0.9	0.5
G22.35+00.41C	0.65	2.62	5.7	5.1	1.7	652	209	2047	733	0.7	0.3	0.2	0.1
G24.55-00.53A	0.12	0.64	0.7	0.8	2.3	48	21	152	70	4.5	2.1	1.4	0.7
G22.56-00.20D	0.24	0.40	1.7	0.7	5.7	63	22	197	77	4.6	1.9	1.5	0.6
G24.60+00.08B	0.13	0.39	1.1	0.7	5.3	43	19	136	63	2.3	1.1	0.7	0.4
G25.04-00.20B	0.18	0.54	1.0	0.7	3.0	23	13	73	43	9.8	5.9	3.1	2.0
G25.04-00.20F	0.14	0.39	0.9	0.6	3.3	21	11	67	36	5.0	2.7	1.6	0.9
G26.99+00.20A	0.52	1.35	4.4	2.6	2.5	349	122	1096	422	1.2	0.5	0.4	0.2
G26.99+00.20E	0.07	0.35	0.4	0.5	7.1	60	26	189	86	9.2	4.4	2.9	1.5
G28.23-00.19C	0.36	1.40	2.6	2.3	2.0	219	82	686	279	2.0	0.8	0.6	0.3
G28.37+00.07D	0.23	1.05	2.0	2.1	5.2	224	81	704	278	2.7	1.1	0.9	0.4
G28.37+00.07F	0.40	1.29	3.6	2.7	4.2	290	104	910	358	1.6	0.7	0.5	0.2
G28.37+00.07G	0.44	1.16	3.9	2.3	3.2	263	96	825	328	1.1	0.4	0.3	0.2
G28.38-00.11A	0.17	0.37	0.7	0.4	3.1	28	26	88	82	8.6	8.2	2.8	2.6
G28.53-00.25D	0.08	0.32	0.6	0.5	4.5	18	10	58	33	4.9	2.9	1.5	0.9
G31.22+00.01A	0.36	1.11	3.2	2.3	3.8	219	87	688	293	1.4	0.6	0.4	0.2
G31.97+00.07B	0.35	1.01	2.7	1.8	4.8	240	95	753	320	4.6	2.0	1.5	0.7
G34.34-00.72A	0.35	0.54	2.3	0.8	1.7	1	3	2	8	9.8	43.5	3.1	13.9
G34.37-00.95C	0.01	0.43	0.0	0.4	2.9	0	0	1	5	69.7	237.7	22.2	75.8
G35.14-00.02A	0.19	0.59	1.3	0.9	1.9	9	10	30	33	3.5	3.9	1.1	1.3
G36.67-00.11A	0.39	1.09	3.4	2.2	2.6	104	59	327	192	1.2	0.7	0.4	0.2
G38.33-00.81A	0.04	0.39	0.3	0.7	3.7	2	5	6	15	5.1	12.5	1.6	4.0
G38.77+00.78A	0.10	0.23	0.6	0.3	4.1	4	4	12	12	12.6	12.6	4.0	4.1
G38.92-00.33A	0.16	0.94	0.8	1.1	2.3	20	17	62	56	14.9	13.5	4.8	4.4
G38.95-00.47A	1.03	2.99	10.1	6.7	2.4	214	157	672	505	1.0	0.8	0.3	0.3
G48.52-00.47A	0.00	0.38	0.0	0.4	4.4	7	8	23	26	31.6	36.5	10.1	11.7

Table C.4: List of sources without detectable ammonia (1,1)-inversion transition. The table contains the names and coordinates in Galactic Longitude l and Galactic Latitude b .

Source	Galactic Longitude l	Galactic Latitude b
	deg	
G15.00+00.79A	15.03	0.80
G17.33+00.88B	17.42	0.90
G17.33+00.88C	17.42	0.87
G17.81+02.02A	17.81	2.02
G17.90+02.05A	17.90	2.06
G19.39-00.01A	19.40	-0.01
G19.42-00.08A	19.40	-0.08
G19.55+00.60A	19.53	0.61
G19.60-01.29A	19.60	-1.31
G19.76-01.25A	19.77	-1.26
G22.00+00.35A	22.01	0.36
G22.13+00.47A	22.08	0.49
G22.40-00.47A	22.41	-0.49
G22.56-00.20A	22.56	-0.22
G22.56-00.20B	22.53	-0.19
G22.56-00.20C	22.57	-0.24
G22.56-00.20E	22.51	-0.25
G23.22-00.37B	23.23	-0.39
G23.26-00.85A	23.22	-0.86
G23.32+00.04A	23.32	0.05
G23.42-00.52B	23.44	-0.53
G23.47+00.10A	23.47	0.10
G23.71-00.20A	0.00	0.00
G23.75-01.26A	23.76	-1.26
G23.79+00.00A	23.79	-0.01
G24.08+00.32A	24.09	0.35
G24.33+00.11A	24.33	0.11
G24.49-00.69B	24.48	-0.71
G24.60+00.08C	24.58	0.10
G25.04-00.20A	24.97	-0.17
G25.10-00.43A	25.12	-0.41
G25.40-00.64A	25.39	-0.59
G25.40-00.64B	25.40	-0.61
G25.63-00.32A	25.66	-0.34
G26.43-00.66A	26.43	-0.66
G26.46-00.40A	26.45	-0.40
G26.48+00.71B	26.45	0.72
G26.99+00.20C	26.90	0.21
G26.99+00.20D	26.99	0.22
G26.99+00.20F	27.12	0.17
G27.01-00.70A	27.00	-0.75
G27.01-00.70B	27.01	-0.69
G27.15+00.54A	27.15	0.53
G27.15+00.54B	27.20	0.58
G27.43-00.71A	27.43	-0.71
G27.77+00.82A	27.76	0.82
G27.84+00.02B	27.87	0.09
G27.84+00.02C	27.86	0.11
G27.84+00.02D	27.91	0.07
G27.84+00.02E	27.85	-0.04
G27.97-00.42A	27.97	-0.42
G28.08+00.07A	28.09	0.07
G28.23-00.19B	28.20	-0.20
G28.37+00.07A	28.34	0.06
G28.51-00.38A	28.51	-0.38
G28.51+03.60A	28.51	3.60
G28.67+00.13A	28.66	0.14
G28.67+00.13B	28.71	0.14

continued on next page

<i>continued from previous page</i>		
Source	Galactic Longitude l	Galactic Latitude b
	deg	
G28.95-00.47A	28.96	-0.47
G29.27-00.71C	29.28	-0.77
G29.27-00.71D	29.31	-0.61
G30.12-01.13A	30.12	-1.14
G30.13-00.62A	30.13	-0.65
G30.14-00.06A	30.14	-0.08
G30.66+00.04A	30.66	0.04
G30.71+00.14A	30.70	0.12
G30.71+00.14B	30.75	0.10
G30.85+00.21A	30.84	0.17
G30.97-00.14A	30.98	-0.15
G31.02-00.10A	31.02	-0.12
G31.03+00.26A	31.01	0.27
G31.38+00.29A	31.39	0.30
G31.99-00.64A	32.00	-0.67
G32.54-00.50A	32.55	-0.50
G32.66+00.50A	32.66	0.51
G33.16-00.54A	33.15	-0.55
G33.16-00.54B	33.17	-0.54
G33.69-00.01C	33.70	-0.01
G33.69-00.01D	33.64	-0.06
G33.69-00.01E	33.62	-0.04
G34.24-01.25A	34.25	-1.26
G34.24+00.13M	34.24	0.13
G34.37-00.95B	34.36	-0.92
G34.37-00.95E	34.37	-1.01
G34.41-00.71A	34.42	-0.73
G34.91+00.13B	34.91	0.13
G35.13-00.83A	35.14	-0.84
G35.24-00.80A	35.26	-0.79
G35.33+00.12B	35.32	0.16
G35.36+00.97A	35.36	-0.97
G35.39-00.33D	35.43	-0.35
G36.34-00.08A	36.35	-0.09
G36.94+00.91A	36.94	0.92
G37.49-00.70A	37.48	-0.72
G37.84-00.07A	37.84	-0.09
G38.81+00.78A	38.82	0.79
G38.82-00.46A	38.85	-0.51
G40.95-00.16A	40.96	-0.16
G40.95-00.25A	40.95	-0.26
G41.01-00.15A	41.02	-0.14
G48.77-00.13A	48.75	-0.11
G48.84-00.32A	48.85	-0.33
G48.93-00.49A	48.93	-0.50
G49.04-00.02A	49.07	-0.03
G49.17-00.07A	49.17	-0.07
G49.18+00.04A	49.18	0.05
G49.25-00.05A	49.26	-0.04
G49.55+00.00A	49.60	-0.01
G49.55+00.00B	49.54	-0.01